Ice nucleating particle connections to regional Argentinian land surface emissions and weather during the Cloud, Aerosol, and Complex Terrain Interactions experiment

B. Testa[1,5], T. C. J. Hill[2], N. Marsden[3], K. R. Barry[2], C. C. Hume[2], Q. Bian[2], J. Uetake[2], H. Hare[2], R. J. Perkins[2], O. Möhler[4], S. M. Kreidenweis[2], P. J. DeMott[2]

[1]Department of Physics and Chemistry, University of Lyon, Lyon, France.

[2]Department of Atmospheric Science, Colorado State University, Fort Collins, CO.

[3] Department of Earth and Environmental Sciences, The University of Manchester, Manchester, GB.

[4] Karlsruhe Institute of Technology (KIT), Institute of Meteorology and Climate Research, Karlsruhe, Germany.

[5] Now at Department of Environmental Systems Science, ETH Zürich, Zürich, Switzerland.

Corresponding author: P. J. DeMott; Paul.Demott@colostate.edu

Key Points:

- Biological components dominated ice nucleating particles active > -20 °C, and those active > -15 °C were enhanced by rain or high RH events.
- Non-heat-labile organic components dominated the activity of ice nucleating particles below -20 °C, exceeding mineral contributions.
- Ice nucleating particle composition and characteristics suggested the majority originated from regional agricultural soils.

Abstract

Here we present a multi-season study of ice nucleating particles (INPs) active via the immersion freezing mechanism, which took place in north central Argentina, a worldwide hotspot for mesoscale convective storms. INPs were measured untreated, after heating to 95 °C, and after hydrogen peroxide digestion. No seasonal cycle of INP concentrations was observed. Biological INPs (denatured by heat) dominated the population active at -5 to -20 °C, while non-heat-labile organic INPs (decomposed by peroxide) dominated at lower temperatures, from -20 to -28 °C. Inorganic INPs (remaining after peroxide digestion), were minor contributors to the overall INP activity. Biological INP concentration active around -12 °C peaked during rain events and under high relative humidity, reflecting emission mechanisms independent of the background aerosol concentration. The ratio of non-heat-labile organic and inorganic INPs was generally constant, suggesting they originated from the same source, presumably from regional arable topsoil based on air mass histories. Single particle mass spectrometry showed that soil particles aerosolized from a regionally-common agricultural topsoil contained known mineral INP sources (K-feldspar and illite) as well as a significant organic component. The INP activity observed in this study correlates well with agricultural soil INP activities from this and other regions of the world, suggesting that the observed INP spectra might be typical of many arable landscapes. These results demonstrate the strong influence of regional continental landscapes, emitting INPs of types that are not yet well represented in global models.

Plain Language Summary

The Cloud, Aerosol, and Complex Terrain Interactions campaign studied how extreme thunderstorms above the Sierras de Córdoba range of Argentina form in dependence on meteorology, local terrain and particles that feed cloud formation. We studied rare ice nucleating particles, which act as seeds for snow crystals (without them, water droplets supercool to -38°C before spontaneously freezing). This freezing begins the process of rain (starting as snow) and hail precipitation. To measure the numbers of atmospheric ice nucleating particles, we filtered air, suspended all collected particles in water and cooled aliquots of suspensions until they froze. To characterize their origin, we heated suspensions to deactivate biological particles (proteins, fungi, bacteria) and retested freezing. Then we digested with hydrogen peroxide to remove all organic molecules (e.g., from windblown soil organic matter) and retested freezing. What remained were inorganic ice nucleating particles (e.g., mineral dust). Biological types froze first at -5°C, and accounted for most ice nucleating particles down to -20°C. Their concentrations were enhanced by rainfall and high humidity. Other organic particles predominated below -20°C, always exceeding the contribution from inorganics. These composition and freezing properties suggested most came from regional agricultural soils, thus connecting human land activities to regional weather.

1 Introduction

Ice nucleating particles (INPs) play a significant role in climate. By facilitating the formation of ice and mixed-phase clouds at temperatures above -38 °C, below which clouds can also freeze homogeneously, INPs are central to the hydrological cycle since they trigger ice phase processes that impact the largest proportion of precipitation on Earth, especially over land (Mülmenstädt et al., 2015). They also impact radiative forcing by modifying cloud optical properties (DeMott et al., 2010).

In this paper, we report on a 7-month survey, from austral spring to mid-fall, of INP measurements at a surface site during the Department of Energy, Atmospheric Radiation Measurement user facility's Cloud, Aerosol, and Complex Terrain Interactions (CACTI) experiment (Varble et al., 2021). This study took place in 2018/2019 in the region over and to the east of the Sierras de Córdoba, part of the Sierra Pampeanas mountain chain that runs parallel to the Andes in Northwest Argentina. The Córdoba province lies in one of the hotspots in the world for mesoscale convective storms and severe storms (Rasmussen et al., 2014; Zipser et al., 2006). Being surrounded by grass and herbaceous plant communities, shrubland, pasture, pine plantation, low forest, arable lands, as well as salt flats and one large city to the north, there are many potential sources of particle emissions to be ingested by and interact with storms. Winker et al. (2013) identified the region as a consistent source of dust, peaking in September to November. Few INP studies have been reported from South America, and to our knowledge, only two within this region, specifically within the city of Córdoba (López and Ávila, 2013; López and Ávila, 2016). Since the mix of arable and natural ecotypes represents a South American analogy to the United States High Plains region, with higher terrain to the west that plays a role in storm generation over a wide region, the study provided the opportunity to examine in detail the sources and activation properties of INPs for comparison to other such continental interior regions where warm season convective storms occur.

Aerosols of all types can impact deep convective cloud properties, both microphysically as cloud condensation nuclei (CCN) and INPs, but also via feedbacks on cloud dynamics. Quantifying these impacts has proven difficult. Even if restricted to examining single storm systems, aerosol-cloud-precipitation interactions can depend on a host of thermodynamic and dynamical factors that include the environmental humidity, vertical wind shear, and convective available potential energy (Fan et al., 2009; Khain et al., 2008; Storer et al., 2010; Yu et al., 2007). Specific aerosol factors include the vertical location and concentration of total aerosols (Fan et al., 2018; Fridlind et al., 2004; Marinescu et al., 2017) and the type of INPs present (van den Heever et al., 2006). Aerosol influences on cold pools left from passing storms exert further complex dynamic feedbacks on the organization of mesoscale convective systems (Lee et al., 2008a-b; Storer et al., 2010; Storer and van den Heever, 2013; van den Heever and Cotton 2007).

Both the more numerous CCN and the rare INPs impact convective storm cloud microphysics by controlling ice evolution in supercooled cloud regions and modifying subsequent precipitation. This occurs via the direct impacts of INPs upon primary ice formation, but also via the impact of CCN on droplet size distributions, which affects ice crystal riming and the secondary ice formation mechanisms of rime-splintering and droplet shattering upon freezing (e.g., Field et al., 2017; Keinert et al., 2020; Lauber et al., 2018). Ice crystal numbers and the growth of large ice and liquid hydrometeors can further drive ice-ice collisions and secondary breakup (Phillips et al., 2017; Sotiripoulou et al., 2021), ice crystal aggregation, and collisions between ice and supercooled raindrops. While INPs may represent only 1 in 10^5 or less of all particles (e.g., typically 1 L^{-1} at -20 °C, out of a total of ~10^6 particles L^{-1} in continental regions) they are usually vital in initiating ice as the first step in this complex chain of events leading to precipitation.

A variety of aerosols show a range of efficacies as INPs. Commonly acknowledged INPs are certain minerals emitted as dust, many of which have been studied in the laboratory (Hoose and Möhler, 2012; Kanji et al., 2017; Murray et al., 2012; Ullrich et al., 2017). The general action of mineral INPs as a single class has also been examined using field data (DeMott et al., 2015).

Prominent amongst atmospherically-relevant minerals is microcline, a specific type of alkali feldspar (K-Feldspar), a minor mineral by mass, but deemed to be the most efficient for ice nucleation, and the basis for a specific parameterization (Atkinson et al., 2013) used within global models (Vergara-Temprado et al., 2017). While mineral INPs are typically discussed as important contributors only at temperatures below -15 °C, few have been quantified over a sufficient range of temperatures and expected atmospheric sizes to be ruled out at any supercooled temperature. It is clear from recent studies that occurred in proximity to major desert regions, that dusts emanating from these regions possess activities as INPs that are greatly enhanced compared to background conditions, even at temperatures higher than -15 °C (Chen et al., 2021; Price et al., 2018).

The least well-defined sources, ones that may equal or exceed the combined contributions of mineral and other inorganic INPs, are organic INPs that may be intact organisms or their products (e.g., cell-free ice nucleating proteins), or the stable products of decomposition or humification. We will refer to these, respectively, as "biological" and "other organic" INPs. Biological INPs are often noted as predominating at temperatures above -15 °C (DeMott and Prenni, 2010; Kanji et al., 2017). Certain species of bacteria and fungi are well known to be efficient ice nucleators (see Després et al., 2012; Fröhlich-Nowoisky et al., 2016; Huang et al., 2021), as are pollens from a range of tree and grass species (Diehl et al., 2002; Gute and Abbatt, 2020; Pummer et al., 2012). However, there are many other potential organic sources, such as from cellular exudates (Hill et al., 2016; Ladino et al., 2016; Wilson et al., 2015), biomass burning (McCluskey et al., 2014; Schill et al., 2020), plant tissues (Hill et al., 2016; Hiranuma et al., 2019; Suski et al., 2018), sea spray (DeMott et al., 2016; McCluskey et al., 2018) and as yet unresolved components within the soil organic matter (Conen et al., 2011; Hill et al., 2016; O'Sullivan et al., 2014; Tobo et al., 2014). Air masses arriving from the surrounding diverse rural ecotypes could introduce biological and other organic INPs into the CACTI region. Arable lands are expected to be a major source (Garcia et al., 2012; Hill et al., 2016, 2018; Suski et al., 2018; Tomlin et al, 2020). Urban aerosols may also be a source of organic INPs, though their efficacy as ice nucleators is presently unresolved. Episodic fluxes would be expected from thunderstorm outflows (Langer et al., 1979) and from the stimulation of INP emissions by precipitation and/or high relative humidity (Huffman et al., 2013; López and Ávila, 2016; Prenni et al., 2013; Tobo et al., 2013; Wright et al., 2014).

While several mechanisms cause the formation of ice crystals in clouds, immersion freezing of INPs appears to be the most relevant process for the mixed-phase region of clouds (de Boer et al., 2011; Kanji et al., 2017; Murray et al., 2012), and is especially expected within the updrafts of convective storms that typically have cloud base temperatures well exceeding 0 °C. For this reason, INP measurements in CACTI focused on immersion freezing. Bulk particle samples were collected with filters, and particle resuspensions were processed to determine immersion freezing INP concentrations (DeMott et al., 2018; Suski et al., 2018). Suspensions were measured untreated, and following exposure to physico-chemical treatments to differentiate between the biological, other organic, and total inorganic INPs. Measurements of aerosol distributions and meteorology were used to investigate the relation between INPs and environment. In particular, laboratory studies of soil dust aerosols generated from topsoil from the same soil unit that underlies extensive croplands to the east of the site (DeMott et al., 2018; Steinke et al., 2016) have been extended by using single-particle mass spectrometry to characterize particle composition and mixing state, to explore the potential relationships to observed INPs.

These analyses were used to evaluate the hypothesis that INPs feeding convective cloud systems over the central Argentinian region are dominated by biological particles and other organic ice nucleating entities that emanate from surrounding regions. We also investigate seasonal cycles, the impact of rain upon emissions, what the data indicate about the organic and mineral sources of INPs in this region, and relations between INPs and other aerosol properties that can inform development of parameterizations.

2 Site Description and Methods

2.1 Regional landscape and climate of the CACTI study area as relevant to INP emissions

The Sierras Pampeanas comprises uplifted basement rocks of the South American continental crust (Steenken et al., 2006, 2010), and as such contains igneous and metamorphic rocks of felsic composition, that are enriched in the lighter elements such as silicon, oxygen, aluminum, sodium, and potassium. The rocks of the Sierra de Córdoba and neighboring Sierra de San Luis consist of large granitoid blocks and schists that had been uplifted during the Cretaceous period (145 - 66 mya) and have eroded into the surrounding lowlands since at least the Neogene period (23 - 2.6 mya), but probably much earlier (Bense et al., 2017). Surface sediment in the modern-day lowlands consist of Holocene loessical sediments with variable volcanic ash contents (Teruggi, 1957), where argillized lithic and feldspar silt-sized fragments from the crystalline basement and detrital illite derived from weathered acidic volcanic material have been transported by wind and fluvial action (Bonorino, 1966). A widespread layer of volcanic ash was deposited on the lowlands after the 1932 Quizapu volcano eruption which was subsequently tilled into the agricultural soils (Hepper et al., 2006).

The province of Córdoba includes a large diversity of natural landforms and lands modified by human activities. Its northwest side is bounded by the eroded Sierras de Córdoba mountain range, while the eastern two thirds is mostly an intensively-farmed plain planted predominantly with corn (Zea mays) and soybean (de Abelleyra et al., 2019, "Mapa Nacional de Cultivos campaña 2018/2019, INTA"). Roughly 200 km north of the measurement site are the extensive Salinas Grandes salt flats, while to the north-east lies Argentina's largest natural salt lake, Laguna Mar Chiquita. Córdoba, Argentina's second largest city (population ~1.5 million), lies 90 km north-east of the measurement site, and Villa Yacanto, a small town of only ~1,000 people, is 3 km to its north-west (Fig. 1).

Córdoba belongs within the Chaco Phytogeographical Province, a large tropical region of central South America that includes semi-arid forest and woodlands, savannas, and shrub/grassland steppes. In the general region surrounding the CACTI study there is mainly Mountain Chaco to the north, and Espinal units to the east (Cabrera, 1976); the natural Espinal forest is now almost entirely lost to agriculture. To the immediate north, west and south of the measurement site, tussock grass and herbaceous plant communities, which can also occur with shrubs, predominate (types A and B in Giorgis et al., 2017), as well as mountain Chaco open and low to medium tall shrubland (Cabido et al., 2018). Interspersed between these natural plant communities are areas of low-input pasture (Fig. S1b) and pine plantation. To the immediate east of the site, pasture and open remnants of fire-ravaged pine plantations grade into a mix of mountain Chaco shrubland and mountain Chaco low forest overlying an open shrub layer (Cabido et al., 2018). A wildfire in the Calamuchita Department in September 2013, with Villa Yacanto at the center, burnt almost

all the land surface for 20 km north and west of the site, and extended roughly 5 km to the east and south.

The Córdoba province possesses a humid subtropical climate. There are modest differences in temperature and humidity between seasons, and rain falls mainly in summer between October and March. The average temperature in spring is around 17 °C, descending to 10 °C at night and up to 30 °C in the day. In summer, the temperature is slightly higher, i.e., 20 °C on average, while in fall, the average is 15 °C. As already mentioned, the region is one of the world's hotspots for mesoscale convective storms and severe storms. During the campaign, several thunderstorms were recorded, generally accompanied by strong winds, up to 72 km h^{-1}. Precipitation was frequent in the region with both strong (e.g., 110 mm in 1 hour) and persistent (e.g., 80 mm over 17 h) events. Rain events were associated with persistently high relative humidity (RH), which averaged 69% during spring, 78% in summer and 76% in fall.

2.2 Sampling Site and Instrumentation

INP measurements at the Department of Energy's Atmospheric Radiation Measurement Mobile Facility 1 (AMF1) captured an extended seasonal cycle of INPs over Austral Spring to mid-Fall. The AMF1 site was located near Villa Yacanto, Argentina, approximately 20 km east of the highest ridge top in the Sierras de Córdoba range at an elevation of approximately 1150 m. The filter sampler was mounted atop the Aerosol Observing System trailer (32.126306°S, 64.728514°W, 4.2 m above ground) (Fig. S1a). Single-use, open-faced, sterile plastic filter units (Nalgene, cat. no. 130-4045) fitted with 0.2 μm pore, 47-mm Nuclepore polycarbonate filters (Whatman, GE Healthcare) were mounted beneath a stainless steel rain shield. Prior to the study, the filters were pre-cleaned and pre-sterilized in a laminar flow cabinet to remove all biological and other organic particles. They were soaked in 10% H_2O_2 for 10 min, followed by three rinses in deionized water (DI), with the final rinse filtered through a 0.1 μm pore syringe filter (Whatman Puradsic, GE Healthcare). After filter loading, the units were packed in plastic slider bags within the laminar flow cabinet for cleanliness during transport. Filters were typically drawn for an 8-hour period, totaling 6000 L sampled on average, and measured with a mass flow meter (TSI model 4043). Filters were removed using cleaned plastic forceps (Fine Science Tools) and stored in sterile petri dishes (Pall). Eighty-three sample filters were collected over 7 months, including 6 blanks (installed with no flow) at intervals throughout the project. Filters were stored temporarily in a -20 °C freezer at the site prior to their return to Colorado State University (CSU) in a dry nitrogen shipper (Cryoport) and stored frozen until subsequent analyses.

The Aerosol Observing System (AOS) at AMF1 included various aerosol instruments. Of special relevance to this study were an aerodynamic particle sizer (APS, 3321, TSI, Inc.) measuring concentrations of particles with aerodynamic diameters from 0.5 to 20 μm; an ultra-high-sensitivity aerosol spectrometer (UHSAS, Droplet Measurement Technologies) which is an optical-scattering, laser-based, aerosol particle spectrometer detecting particles with optical diameters from 0.06 to 1 μm; an SMPS (classifier model: 3080 and DMA model: 3081, TSI, Inc.) measuring particles with mobility diameters from 0.013 to 0.5 μm; and a nephelometer (Model 3563 Nephelometer, TSI, Inc.) measuring scattering signal from bulk particles at three wavelengths (450, 550 and 700 nm) and mounted with alternating 1 μm and 10 μm impactors at the aerosol inlet (Uin et al., 2019). Aerosols were dried upstream from the SMPS and UHSAS while the APS measured particles at the humidity within the aerosol inlet in the AOS trailer (see Uin and Smith (2020) for a description of the AMF1 AOS). The nephelometer system in AMF1

is a humidigraph, with two nephelometers in series. The first nephelometer sampled at ambient RH in the trailer, while the second measured at elevated RHs imposed by a drying/humidification system immediately upstream; this study used data from the first, ambient-RH nephelometer. No correlations were found between the scattering signal from particles larger than 1 μm and ambient relative humidity, suggesting that the overall coarse particles sampled at the AMF1 site (e.g., by the APS) were fairly hydrophobic, with sizes close to their dry diameter. Meteorological measurements associated with the AOS are ambient temperature, pressure, relative humidity, wind speed and direction and precipitation (measured by a piezoelectric precipitation sensor; Kyrouac, 2019).

The aerosol size distribution was merged (i.e., leading to a continuous size distribution that encompasses all size distribution measurements) following Hand and Kreidenweis (2002) and Khlystov et al. (2004). The method is described in the Supporting Information. Hereafter, we assume the resulting size distribution represents dry particles. Since APS data were only available from October 23 to December 31, 2018, nephelometer measurements were used outside of this period to derive supermicron aerosol surface areas, as described in the Supporting Information.

Complementing ground-based observations, the Department of Energy Atmospheric Radiation Measurement Program Aerial Facility G-1 (Gulfstream−I) aircraft measurements provided the unique ability to capture INPs above the surface layer at the AMF1 site. Research flights were conducted from November 4 to December 8, 2018. During this period, INP measurements were done every week after the flights at the AMF1 site. Some results from the aircraft measurements are presented in Varble et al. (2021) but have not been investigated in this study.

2.3 Measurement of ice nucleating particles

All INP temperature spectra were obtained from suspensions of the filter-collected particles in DI water using the CSU Ice Spectrometer (IS). The IS is constructed using two aluminum blocks, machined to fit polymerase chain reaction (PCR) plates, encased by cold plates through which coolant is circulated. The IS produced immersion freezing spectra reaching to a lower limit of -27 to -30 °C with a detection limit of ~0.001 INPs L^{-1} and is supported with well-established experimental protocols applied in diverse scenarios (Barry et al. 2021; Beall et al., 2017; DeMott et al., 2017; Hill et al., 2016; Hiranuma et al., 2015).

To re-suspend particles, sample filters were placed into sterile 50 mL polypropylene centrifuge tubes (Corning), 7 or 8 mL of 0.1 μm-filtered (Whatman Puradisc) DI water was added and the tubes were tumbled end-over-end for 20 min. Thirty-two aliquots of 50 μL of each sample, plus several serial dilutions, were dispensed into PCR trays (OPTIMUM® ULTRA, Life Science Products) in a laminar flow hood and placed into the cooling blocks. The headspace was purged with HEPA-filtered N_2 (750 mL min^{-1}). The IS, and headspace N_2, were cooled at 0.33 °C min^{-1} using a recirculating low temperature bath, and the freezing of wells recorded through a LabVIEW interface with a charge-coupled device camera system. Freezing fraction results were corrected for INPs in the 0.1 μm-filtered DI using a sample blank array.

Background contamination on filters was determined using the average INP spectra from field blanks (lids were removed from Nalgene units on site before being replaced, then the filter was removed and stored). The average number of INPs per filter on blanks were then subtracted from

the calculated number of INPs per sample filter before conversion to concentration. Immersion freezing temperature spectra were obtained by converting the number of frozen wells at each temperature to the number of INPs mL^{-1} suspension using Eq. 13 in Vali (1971), and then converted to concentration per standard liter of air (0 °C and 1013.25 mb) from the volume collected. Ninety-five percent confidence intervals for binomial sampling were obtained from Eq. 2 in Agresti and Coull (1998).

Tests were performed on selected suspensions to estimate the contributions of heat-labile INPs (e.g., proteins), hereafter called "biological INPs". Two milliliters of suspension were heated to 95 °C for 20 min and the sample re-analyzed in the IS to gauge the reduction in INP concentrations (Hill et al. 2016; O'Sullivan et al., 2018).

Tests were also performed to quantify INPs that were organic but heat stable, such as most INPs in soil organic matter (Hill et al. 2016). Hereafter, these are termed "other organic INPs". Their abundance was assessed by digesting 2 mL of suspension after addition of hydrogen peroxide to a final concentration of 10%, at 95 °C for 20 min under UV-B. This procedure, and the neutralization of remnant H_2O_2 to prevent freezing point depression, are detailed in Suski et al. (2018). The sample was then re-analyzed to assess the reduction caused by the decomposition of all organic INPs. The difference between INPs remaining after the heat treatment and this measure of all organic INPs provided an estimate of the other organic INPs.

INPs remaining after peroxide digestion were deemed to be inorganics. Atypically, after H_2O_2 treatment, a few INP spectra showed a persistent minor "hump" of activity above -20 °C. An extended digestion for 40 min only modestly reduced the size of the residual hump (Fig. S4). Mikutta et al. (2005) noted that peroxide digestions of soil were typically incomplete due to protection of organic matter within aggregates and their adsorption on mineral surfaces, and the inability to oxidize organo-mineral complexes and chemically-resistant compounds such as pyrogenic materials (black carbon) and aliphatic hydrocarbons. The INPs contributing to the hump after the extended digestion could also be minerals further affected by their extended immersion in boiling water. Such sensitivity of mineral INPs was recorded in Harrison et al. (2019), but was not of concern here since inorganic INPs were of minor importance in the affected temperature range, as described later in the results. Thus, the INPs remaining after H_2O_2 treatment were considered as entirely "inorganic". Concentration differences between the three INP classes were computed only if they were statistically significant ($p < 0.05$), tested using Fisher's Exact Test (Sprent, 2011) on the number of frozen and unfrozen wells in IS tests.

Measurements of INPs were also performed on an Argentinian soil sample. An aerosolized suspension of Argentinian soil dust collected from the Pampas region (hereafter "SDAr01"), was previously analyzed in two laboratory studies, by Steinke et al. (2016) and by DeMott et al. (2018) during the ice nucleation measurement inter-comparison campaign FIN-02 (Fifth international workshop on Ice Nucleation - phase 2). The soil sample was collected from the Anguil Experimental Station (INTA) in a cornfield (36.57675°S, 63.98795°W) under continuous agricultural use (Siegmund et al., 2018). While the soil samples were taken 499 km SSE of the AMF1 site (Fig. 1), the soil unit to which they belonged, a loamy sand/sandy loam, classified as a coarse haplic kastanozem (Kh1-1a; FAO, 1971), also underlies most of the cropped plain that starts ~35 km east of AMF1. From there a 100-300 km wide band of haplic kastanozem soils

extends ~1,500 km to the NNE. A stored (at -20 °C) suspension from the FIN-02 studies in DeMott et al (2018) was recently heat and peroxide treated, as described above, as those tests have not been performed during FIN-02.

2.4 Single-particle mass spectrometry

The Fifth international workshop on Ice Nucleation - phase 1 (FIN-01) was conducted as an intercomparison of the performance of single-particle mass spectrometers for online size resolved composition measurements of single aerosol particles (DeMott et al., 2018). Dry particle suspensions in air were created at the Aerosol Interactions and Dynamics in the Atmosphere (AIDA) chamber facility, Karlsruhe Institute of Technology (KIT), as was also done for FIN-02. The SDAr01 sample was also analyzed during FIN-01. These data are considered of special relevance to regional soil emissions in the CACTI region.

The data presented were obtained by the University of Manchester version of the laser ablation aerosol particle time-of-flight (LAAPTOF) mass spectrometer (Gemayel et al., 2016) whilst in the early stages of development. Single-particle mass spectrometry is an analytical technique in which single particles are directly entrained into a vacuum, isolated by optical detection, vaporized into an ion cloud by laser desorption ionization (LDI) and analyzed by time-of-flight mass spectrometry (TOFMS) (Murphy, 2007). The technique is generally non-quantitative due to matrix effects during LDI (Reinard and Johnston, 2008), but can be considered semi-quantitative with careful calibration against well-defined proxies.

Argentinian soil particles were suspended in the APC (Aerosol Particle Chamber) facility at KIT using a rotating brush generator (RBG 1000), producing distributions as documented in prior studies (DeMott et al., 2018; Steinke et al., 2016). Aerosol was sampled by the LAAPTOF (and other instruments) via a pumped stainless steel sampling line. At the time of the FIN-01 campaign, the instrument was capable of sampling single aerosol particles 0.5 - 2.5 μm in diameter and had a partially developed optical detection system which resulted in an overall detection efficiency of less than 1% (Marsden et al., 2016). Despite this, the instrument provides representative single-particle composition information of the fine fraction of suspended soil and dust samples.

Single-particle mass spectrometry is particularly good at detecting aluminosilicate due to the sensitivity of the technique to silicon, aluminum, alkali metals and earth-alkali metals in the positive ion spectra (Dall'Osto et al., 2010; Gallarvardin et al., 2008). In fact, the mineral phase is defined by the crystal lattice structure required to achieve charge balance between these elements. For example, pure K-feldspar has the formula $KAlSi_3O_8$ to achieve charge balance in a framework crystal lattice. In circumstances where the elemental ratios can be measured quantitatively, pure crystalline mineral phase can be inferred directly from the measurement by calculating the chemical formula, but this is not possible with single-particle mass spectrometry because the required level of quantification is not achievable. However, an assessment of the cation balance relative to pure mineral proxies is an informative assessment of the composition of the aluminosilicate particles in soil, somewhat analogous to cation exchange capacity.

$$Cation\,Balance = \frac{K + Na}{Al + Si} \quad (1)$$

In addition to sub-compositional analysis of cations in mineral dust particles, the U. Manchester LAAPTOF instrument is capable of a single-particle crystal structure analysis using a novel technique that exploits differences in ion formation processes during the ablation of crystalline material (Marsden et al., 2018). This technique exploits a matrix effect that causes a shift in the time of flight of the O- elemental ion (ΔT_O) and the SiO_3- fragment ion (ΔT_{SiO3}) on the negative ion mass scale. Careful examination of mass spectra obtained from nominally pure mineral dust reveals a reproducible peak shift, particularly in potassium- and sodium-bearing phases such as illite, smectite and feldspar, providing a valuable differentiation of minerals that are similar in composition but different in crystal structure.

$$Crystal\,Structure\,(\tau) = \frac{\Delta T_O}{\Delta T_{SiO3}} \quad (2)$$

These analytical techniques were previously applied to nominally pure mineral phases and soil/desert dust from North Africa that were obtained from laboratory-suspended samples during the FIN-01 and INUIT09 (Ice-Nuclei Research Unit programme) campaigns at AIDA (Marsden et al., 2019). These data provide references with which to compare the composition of the aerosolized suspension of the pampas agricultural soil sample SDAr01.

3 Results and Discussion

3.1 Air mass trajectories as indications of aerosol source regions

Three-day air mass back-trajectories were generated with the National Oceanic and Atmospheric Administration Air Resources Laboratory's Hybrid Single-Particle Lagrangian Integrated Trajectory model (HYSPLIT, Stein et al., 2015). Trajectories were initiated every 3 hours, starting 50 m above ground level at the coordinates of the AOS trailer. The area covered by all back-trajectories was meshed into grid cells of 1° longitude/1° latitude. For each back-trajectory, its occurrence in each grid cell was normalized according to the time that the air-mass spent traversing it, and further normalized according to the distance between the grid cell and the AMF1 site (start point), giving a lower weight to grid cells closer to the AMF1 site to remove the "peak" that naturally occurs at the trajectory initiation site (Ashbaugh et al., 1985). The resulting map reveals both where the air mass passed in the 3 days before reaching AMF1 as well as where it spent the most "effective" time. The analysis was performed for the entire period over which filter samples were taken, and then averaged to produce a composite residence-time-weighted trajectory map, shown in Figure 1. Similar maps were produced separately for spring, summer and fall but showed only minor differences (not shown here).

Under the assumption that the particles arriving at AMF1 were more likely emitted from regions where the air masses spent more time, the grid cells showing the highest coefficients in the back-trajectory analysis were considered as the principal particle sources. The regions with the strongest coefficients (orange and yellow in Fig. 1) are located generally east of AMF1,

extending approximately 800 km to the north- and south-east, and 300-500 km to the south, with slightly higher coefficients in the north-east.

For the grid cells with coefficients >5 within 100 km of AMF1, the landscape is comprised of an initial 30-50 km band of mixed vegetation (native grass and herbaceous plant communities, shrublands and low forest, and low-input pasture and pine plantation), which then gives way to corn and soybean cropland. At the north-east perimeter lies Córdoba city. The nearby zone of diverse plant communities will likely emit more biological and other organic INPs from various plants and litter layers than soil dusts from exposed patches and cultivated fields, while the intensively farmed plain may be a principal source of soil dusts from after harvesting to late spring with a mixed source of bio-particles released by plants and soil dusts once the crops emerge. The city will have a complex mixture of transportation, industrial and energy production emissions.

The array of landscape cells with coefficients >5 lying between 100 and 300 km away from AMF1 is again dominated by corn and soybean croplands, as well as some pasture used for raising cattle. To the north-east is the large salt lake, Laguna Mar Chiquita. From 300-500 km, the regions of high coefficients are dominated to the north-east by cattle raising pasture, and to the east and south-east a mix of pasture with corn/soybean cropland. To the east there are also extensive wetlands on the floodplain of the Paraná River Delta (de Abelleyra et al., 2019, "Mapa Nacional de Cultivos campaña 2018/2019, INTA").

Similar normalized residence time analyses were performed for longitude/height and latitude/height (not shown). Both showed that air masses arriving at AMF1 remained below 300 m above ground level (in the planetary boundary layer) during their 3-day back-trajectories. This emphasizes that the surface sources detailed above likely contributed the bulk of the particle burden observed at the site.

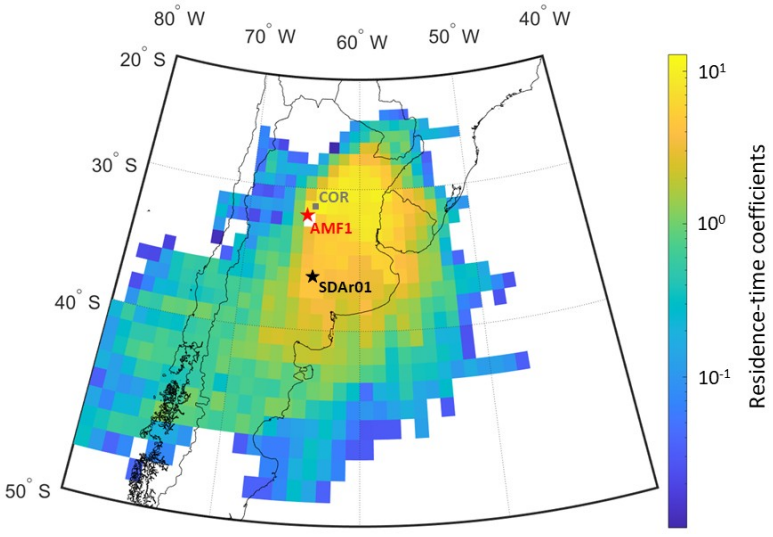

Figure 1. Residence-time-weighted back-trajectories for the period of the campaign. The coefficients of the grid cells encompass, and are weighted by, the time the air mass spent in the cells before arriving at AMF1 (red star on the map) and the distance between the cells and AMF1. Cells with the strongest coefficients indicate likely principal sources of the particles

observed at AMF1. The sampling location of the SDAr01 sample is indicated by the black star and the city of Córdoba by the grey square.

3.2 INP temperature spectra and evolution with time

A time series of total INP concentrations at -25, -20, -15 and -10 °C is shown in Figure 2a. As expected, the higher temperature INPs (above -20 °C) have relatively low concentrations (minimum of ~6×10^{-4} L^{-1} at -10 °C on October 20, 2018) while the lower temperature INPs are almost 7 orders of magnitude more abundant (maximum of ~325 L^{-1} at -25 °C on November 24, 2018). It is clear that INPs active at -25 °C evolve and respond independently from those at -20 and -15 °C, particularly in summer and fall. This suggests different INP populations predominate in each group. The INP concentrations at -20 and -15 °C clearly co-vary, with a mean ratio of about 7. The ratio between INPs at -15 and -10 °C, and between -25 and -20 °C are both about 60, indicating two regions in the spectrum where the INP concentration increases steeply. Both INP classes undergo significant variations over short periods (e.g., in November, during intensive sampling corresponding to the ARM Aerial Facility campaign) reflecting dynamic responses of the INP populations to environmental conditions, or changes in particle sources.

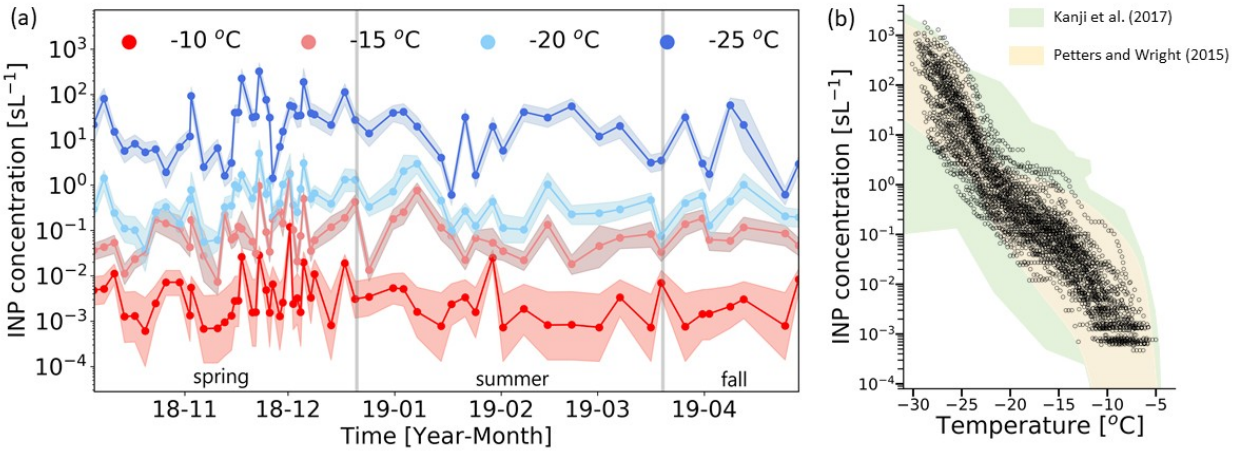

Figure 2. a) Ice nucleating particle concentrations at the AMF1 site during the campaign, at four processing temperatures. The shaded area enclosing each represents the 95% confidence intervals. b) INP spectra of all samples (error bars omitted for clarity). The light green shaded area represents upper and lower limits of global field INP concentration measurements summarized in Kanji et al. (2017, Fig. 1-10), while the yellow shaded area represents atmospheric INP concentration ranges estimated from precipitation samples collected in North America, Europe and Antarctica (Petters and Wright, 2015).

The variations in temperature dependence of the ice nucleation ability of the particles is more visible when plotted as ice nucleation activation temperature spectra (Fig. 2b). The range of INP concentrations at each temperature likely reflects the variability of the background aerosol concentration, the diversity of sources, and the impact of local weather upon emissions. The spectral band lies within the range of concentrations measured in many past studies from other parts of the world, as summarized in Kanji et al. (2017), although tending toward the high end of previously reported values below -25 °C. The CACTI spectra also fit centrally between the upper

and lower sigmoidal curves of atmospheric INPs predicted from INP concentrations in precipitation sampled in North America, Europe and Antarctica (Petters and Wright 2015).

The effect of heating the particle suspensions at 95 °C (Figs. 3a and 3b) to remove contributions of biological INPs (e.g., proteins), is remarkable at higher temperatures. It eliminated all detectable INPs above -10 °C in all samples while reducing the concentration at -15 °C by more than an order of magnitude in ~60% of the treated samples. Such reductions in this temperature regime are similar to those found in prior studies conducted in agricultural regions (e.g., Garcia et al., 2012; O'Sullivan et al., 2018; Schiebel, 2017; Suski et al., 2018). At lower temperatures, heat had no statistically-discernable impact. Removal of all organic INPs with peroxide (Figs. 3a and 3b) produced typically 1 order of magnitude additional reduction below -20 °C but had little additional impact at higher temperatures. Therefore, the contribution of organic INPs was substantial at all temperatures, even below -25 °C, revealing that inorganic INPs were a minor proportion of the total. Summarizing the heat and peroxide treatment effects, we can distinguish between three INP populations: above around -22 °C, the INPs are primarily biological; below this temperature, they are predominantly other organics; below around -12 °C, there are relatively minor contributions from inorganic INPs. We note that in particular, below around -22 °C, other organic INPs are up to 25 times more abundant than inorganic INPs.

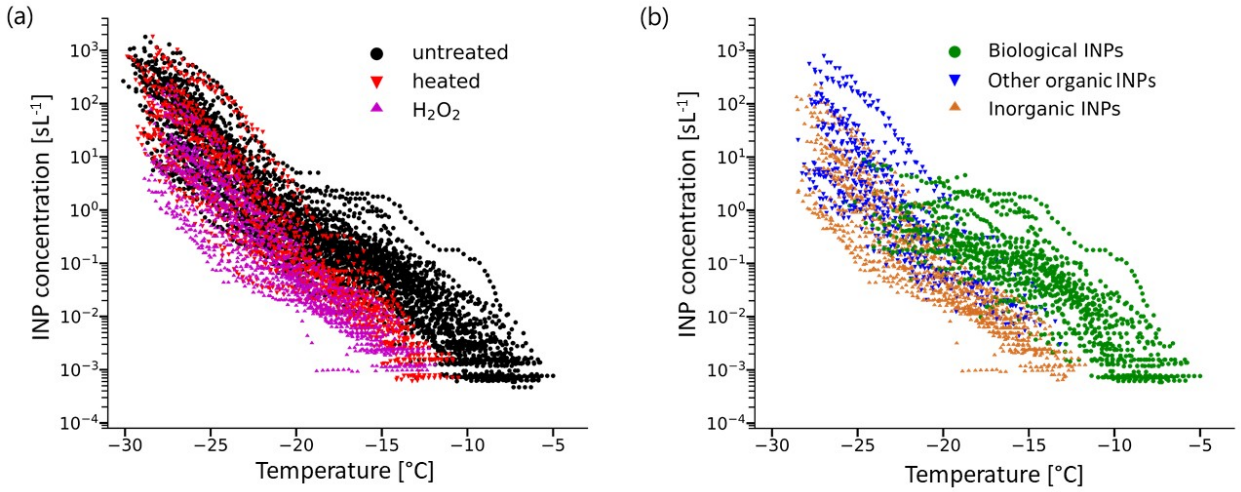

Figure 3. Ice nucleation activation temperature spectra of processed INP samples. a) INP spectra of untreated samples superimposed over INP spectra following heat and H_2O_2 treatments. b) Spectra of computed biological, other organic and inorganic INP contributions derived from statistically significant differences between the untreated and heated spectra, significant differences between the heat-treated and the H_2O_2-digested spectra, and the residual activity remaining after H_2O_2 oxidation (see Section 2.3). Uncertainties are omitted here for clarity, but are shown in Figure 2a.

The profile of each total INP spectrum is the sum of a "hump" of biological INPs and the mostly log-linear distributions of the other organic and inorganic INPs. The inflection point, which lies on average at around -21 °C (Figs. 2b and 3a), identifies the temperature where the concentration of biological INPs equals the combined other organic + inorganic INP contributions for the

employed 8-hour sampling periods. Above this temperature, the INPs are increasingly biological, while below it they are predominantly other organic + inorganic.

Very similar spectra, with inflection points ranging from -18 to -24 °C, can be seen in other studies sampling terrestrial boundary layer air (DeMott et al., 2017; Creamean et al., 2019; Gong et al., 2019; McCluskey et al., 2018; Schiebel, 2017; Suski et al., 2018). Furthermore, a remarkably similar sigmoidal shape, with a two-order-of-magnitude increase between -8 and -20 °C, a three-order increase between -20 and -28 °C, and a change in slope at ~-19 °C, is also evident in the INP spectrum of aerosol generated with Argentinian topsoil sample SDAr01 during the FIN-02 inter-comparison (c.f., Fig. 4 of DeMott et al., 2018). This result will be explored further in section 3.4.3.

3.3 Relation with meteorology and aerosol properties

3.3.1 INPs and meteorology

During CACTI, the INP concentration did not show any apparent seasonal cycle (Fig. 2a). This goes along with the similarity in the seasonal normalized residence time analyses as well as the modest differences in temperature, rainfall and humidity under the region's humid subtropical climate. Alternatively, it may indicate INP populations correlated with factors other than climate. This consistency contrasts with a recent study of INPs in the Finnish boreal forest, where INP concentrations showed a pronounced seasonal cycle reflecting changes in the strength of biogenic sources (Schneider et al., 2020). In CACTI, where the surrounding ecotypes are very heterogeneous and vary according to wind sector, the INP populations may be influenced by a range of factors. These could include current and recent weather, such as precipitation intensity, RH, wind direction and speed. They could also be influenced by agricultural practices, such as topsoil dust generation from plowing, by biological seasonal cycles, such as tree and grass pollen release in spring and summer, and by mushroom growth and spore release in autumn, triggered by rain. From mid-November to mid-December, the concentrations of the higher temperature INPs varied greatly (Fig. 2a) over the short term. Such temporal variability may have been missed in other months when the measurement frequency was lower.

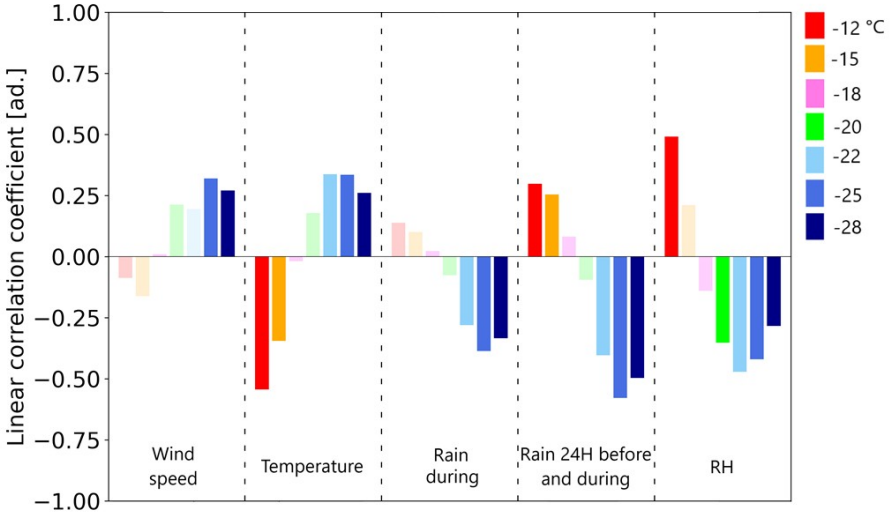

Figure 4. Linear correlation coefficients between the logarithm of the untreated INP concentration and meteorological variables at various processing temperatures. "Rain during" refers to rain occurring during the period of filter sampling, while "rain 24H before and during" refers to rain occurring up to 24 hours before filter sampling as well as during. Pale histogram bars represent non-significant coefficients ($p > 0.05$).

To assess the influence of weather upon INP concentrations, correlation analyses were performed. Figure 4 shows linear correlations (i.e., Pearson correlation coefficients, hereafter "pears") between the $\log_{10}$ of INP concentration and four key meteorological parameters: wind speed, temperature (2 or 3 °C steps), RH, and precipitation. While the INPs were only moderately correlated with the meteorological variables, there were consistent trends of the linear correlation coefficients when progressing from higher to lower temperature INPs. The lower temperature INPs were weakly positively correlated with wind speed, while the higher temperature INPs showed no such correlation. When winds exceed a certain threshold, dust and soil particles (including plant litter) will be lofted, depending on their dryness and friability. This was observed on November 17, 2018 (Fig. 5a), east of the sampling site, when strong SE winds raised dusts from the predominantly bare, recently seeded fields on the farmed plain. Significant anti-correlation of high temperature INPs with temperature, but their positive correlation with RH, indicates that these more-active INPs were more abundant during colder and wetter conditions. By contrast, INPs active at lower temperatures were positively correlated with warmer and drier conditions.

Rain occurring during the period of sampling was significantly negatively correlated with lower temperature INPs, suggesting their effective removal from the boundary layer due to scrubbing and/or the quenching of dust lofting from wetted soils. When considering rain occurring up to 24 hours before the sampling period, this cold INP anti-correlation trend was accentuated, but was also joined by a significant positive correlation between recent moisture and higher temperature INPs. Unsurprisingly, the trends of correlations for RH were similar to those for rainfall. We may note here both consistencies and differences of these results with the findings of López and Ávila (2016) for their studies in Córdoba city. They also found increases in INP concentrations at higher ambient RH and with rainfall, although for ice nucleation in the deposition regime (ice nucleation from supersaturated vapor, where no liquid water is involved; Vali et al., 2015) at -25 °C and below water saturation. The different populations active in the deposition regime, in comparison to immersion freezing, may partly explain the discrepancy with our results at -25 °C, as may the much longer sample integration times and volumes in our studies. Finally, the relatively high correlation between RH and INPs at -12 °C may indicate release mechanisms beyond those induced directly by rainfall, as we will discuss further.

3.3.2 The special effect of rain on the INPs in the CACTI region

When rain occurs, atmospheric particles can be scavenged by Brownian diffusion, phoretic processes and impaction (Pruppacher and Klett, 1997), depending on their size and on the concentration of rain drops. At the same time, although wet soils are less likely to loft dust, rain drop impacts can aerosolize other particle types from surfaces. For example, organic particles or bioaerosols can be generated by the bursting of air bubbles entrained by raindrops impacting the soil (Joung et al., 2017; Wang et al., 2016;). The efficiencies of these mechanisms are known to be driven by several factors such as soil wetness, soil temperature and drop impact speed. Rain impaction on plants is also a likely source of biological INP emissions (Constantinidou et al.,

1990; Huffman et al., 2013; Prenni et al, 2013; Tobo et al., 2013). Moreover, during rain and at high RH, pollen can rupture and release several hundred particles per pollen grain, ranging in size from 0.25 to 1 µm which, depending on the plant species, can act as INPs (Diehl et al., 2002; Gute and Abbatt, 2020; Hughes et al., 2020). Relative humidity is also known to affect INP populations (Huffman et al., 2013; Wright et al., 2014), such as by stimulating the growth of ice-nucleating bacteria on leaves (Hirano et al., 1996) or by inducing wet discharge of fungal spores (Elbert et al., 2007; Hasset et al., 2015).

The intense rainfall and dynamic weather in the Córdoba province drove different responses of immersion freezing INPs active at lower versus higher temperatures, as was evident from their opposite linear correlation coefficients for all meteorological variables, including rain (Fig. 4). Here we investigate the effect of rain on the different INP populations in more detail.

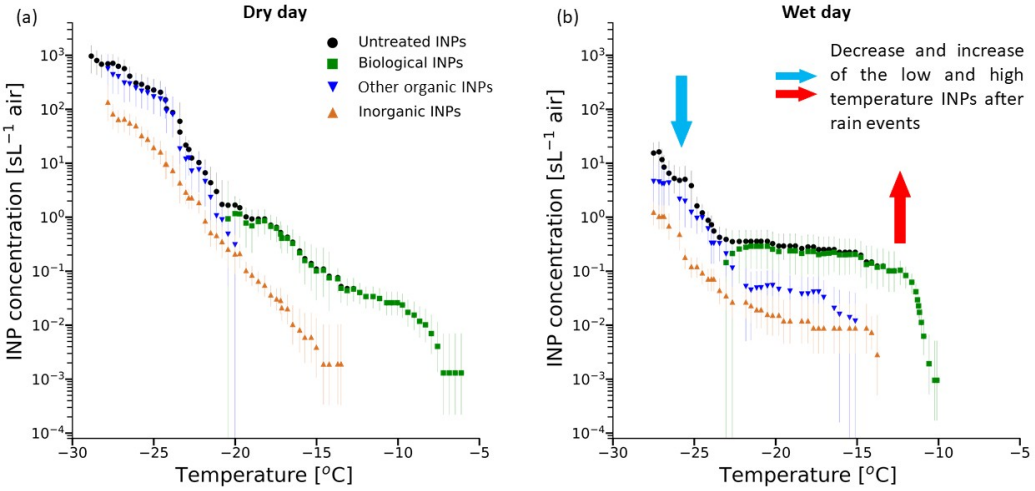

Figure 5. INP spectra for a) a "dry" day (November 17, 2018), i.e., with no rain occurring 24 h before and during the period of sampling, and b) for a "wet" day (November 12, 2018) with RH>80% and precipitation occurring within 24 h before and/or during sampling (on this day, rain occurred 6 h before and during sampling). The effect of rain upon INP populations is generalized by the arrows. Error bars indicate 95% confidence intervals.

Figures 5a and 5b show typical INP spectra under "dry" and "wet" conditions, respectively. Under dry conditions (Fig. 5a), which we defined as RH<80% and with no precipitation 24 h before and during the period of sampling, biological INPs dominated between -5 and -20 °C, with a concentration around 10^{-3} L^{-1} at -5 °C. Their concentrations increased with decreasing temperature up to 1 L^{-1} at -20 °C. Some samples showed high temperature "humps" in the INP spectra indicative of the preponderance of biological particles. The inorganic and other organic INPs showed quasi log-linear spectra for most of the cases (e.g., Fig. 5a), with concentrations up to 10^{2} L^{-1} and 10^{3} L^{-1} at -28 °C, respectively. The wet day (i.e., with RH>80% and precipitation occurring within 24 h before and/or during sampling) (Fig. 5b) corresponded to RH ~100% and 38 mm cumulative rainfall occurring 6 hours before and continuing during sampling, which markedly lowered concentrations of particles >0.1 µm diameter due to wet deposition (see insert in Fig. S5a). Biological INPs increased greatly at temperatures between -10 and -15 °C, including a 2 order of magnitude increase from -10 to -12.5 °C, followed by a plateau between -

15 and -20 °C. In this case, there is also a suggestion of enhanced emissions of other organic and inorganic INPs > -22 °C, although the latter may be an artifact caused by incomplete H_2O_2 digestion, as previously discussed. Concurrently, the concentration of other organic and inorganic INPs at lower temperatures decreased markedly, from 1000 to 5 L^{-1}, and from 100 to 1 L^{-1} at -28 °C, respectively. The blue and red arrows show the generalized rain impact on the INP populations. These results are in agreement with the linear correlation coefficients shown in Fig. 4, and exemplify the opposing responses of the lower temperature immersion freezing INPs compared to the higher temperature INPs in response to rain. Nevertheless, the INP spectra were still consistently dominated by biological INPs from -5 to -20 °C on both dry and wet days.

Such changes in the concentrations of the low and high temperature INPs may be visualized for the entire campaign by computing the ratio of their concentrations at -12 °C ($[INP]_{-12°C}$) and at -25 °C ($[INP]_{-25°C}$) (Fig. 6). The ratio consistently increased during or after precipitation. By including cumulative precipitation occurring both before as well as during the period of sampling, we found that precipitation occurring as much as 24 hours before sampling might explain the increase of $[INP]_{-12°C}/[INP]_{-25°C}$. The slope of the INP concentration between -10 and -12.5 °C (i.e., $slope = \{ln([INP]_{-12.5°C}) - ln([INP]_{-10°C})\} /2.5,$ in K^{-1}) computed for each sample modestly correlated with cumulative precipitations occurring 24 h before and/or during sampling (pears = 0.58 with $p = 8\times10^{-6}$). This moderate but significant correlation suggests that the enhancement of the biological INP concentration during rain events also contributes to the increase of the ratio shown on Fig. 6. Hence, due to the combined enhancement of biological INPs and the reduction of other organic + inorganic INPs active at lower temperatures, the ratio increased by up to 250-fold above the baseline recorded for dry days. When no precipitation occurred before or during INP sampling, the ratio oscillated around a fairly constant value of 0.0002, suggesting there is a typical ratio for "dry" days. During February (mid-summer), precipitation did occur, but not preceding or during INP sampling days. Hence, in that month the recorded ratio of $[INP]_{-12°C}/[INP]_{-25°C}$ stayed at ~0.0002. Moreover, directly after the rain events, in all months, the ratio returned to the pre-rain value within one (the minimum sampling frequency) to 7 days (the period from October 26 to November 2, 2018). On several occasions, a return to the standard dry day ratio of 0.0002 occurred within a day of heavy rainfall (>60 mm). Bigg et al. (2015) recorded higher INP concentrations at -15 and -20 °C the day after heavy rain at several sites in Australia, but observed that they remained raised while exponentially declining for up to 20 days afterward. Such extended effects were not evident in this study.

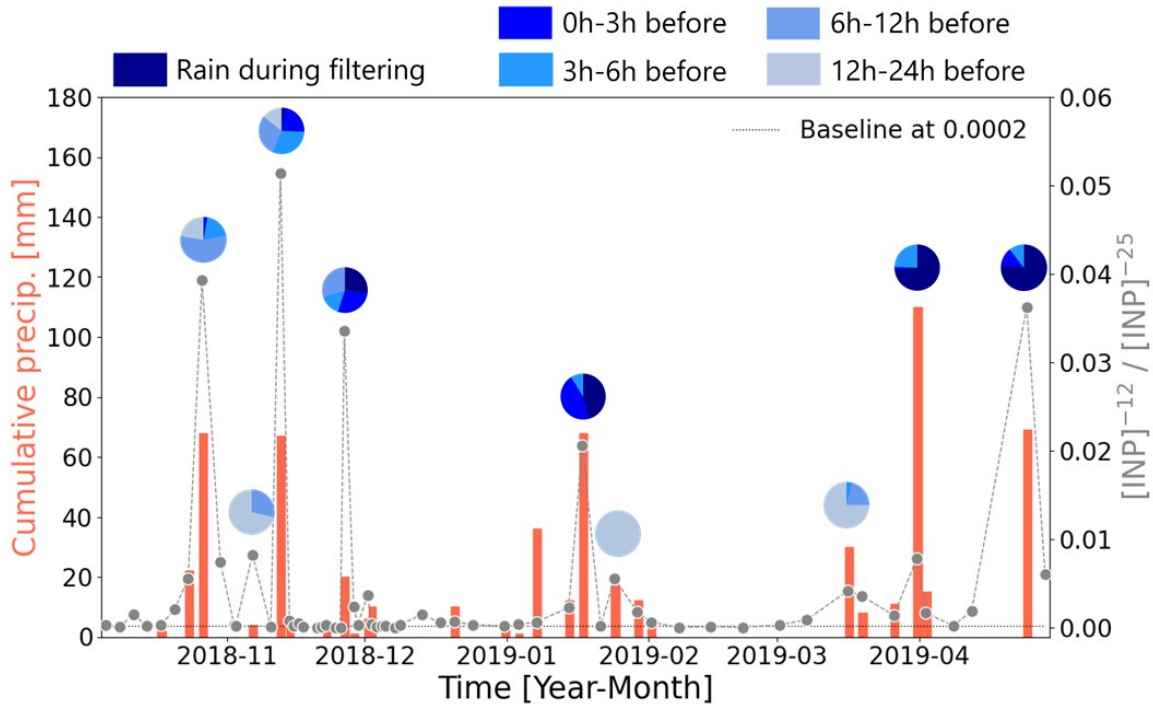

Figure 6. Time series of the ratio of $[INP]_{-12°C}/[INP]_{-25°C}$ (i.e., ratio of concentrations of INPs active at -12 °C with INPs active at -25 °C). Each point represents one INP sample (the dashed grey lines linked the dots for guiding the eye). Total precipitation within 24 hours before and during filter sampling is given by the bars, while the proportions of rain occurring within different timespans are shown by the pie charts. The baseline for dry sampling days is indicated by the dotted line.

3.3.3 Relations between INP types, and with aerosol distributions

In this study, the increase in INPs induced by rain occurred almost exclusively between -10 and -15 °C, with a midpoint at -12 °C. This suggests that the populations of biological INPs active at around -12 °C originated from different sources than biological INPs active at colder temperatures, such as at -20 °C. Figure 7a shows the concentrations of biological INPs active at -20 °C versus aerosol particles with inferred dry diameters greater than 1 µm (N_{sup}), and similarly for INPs active at -12 °C (Fig. 7b). For Fig. 7b, all samples at -12 °C were included, not only those that were heat-treated, because in all processed samples (28 samples) the biological INPs accounted for an average of 98.5% of the total; thus, we assumed that in the non-heat-treated samples (60 samples) the INPs were also essentially all biological. The shape of the points indicates whether sampling occurred during rain or not, while the color shows mean RH.

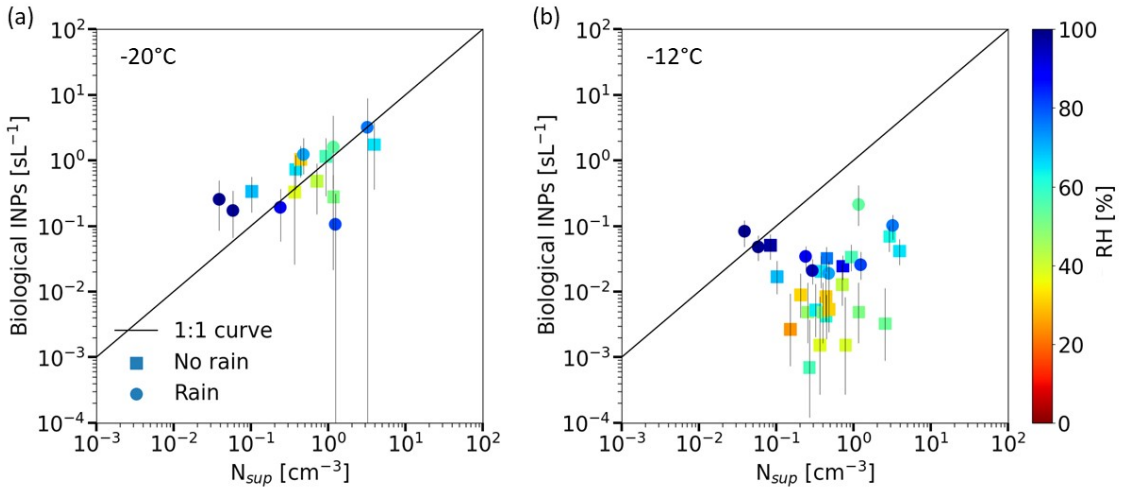

Figure 7. The concentration of biological INPs active at a) -20 °C and b) the concentrations of all INPs (likely all biological) active at -12 °C, versus the concentrations of aerosol particles with a diameter >1 µm (N_{sup}). Circles correspond to filters sampled during rainy days (rain up to 12 h before sampling), while squares indicate non-rainy days. The average relative humidity during sampling is given by the color. Error bars indicate 95% confidence intervals. Lines show 1:1 relationships.

As biological INPs are more likely to be larger particles when intact (e.g., bacteria, fungal spores, and pollen), one would expect their concentrations to be positively correlated with the concentrations of supermicron aerosols. This was observed at -20 °C (Fig. 7a) both during rainy and non-rainy days (pears = 0.87 with p = 0.0048, and 0.73 with p = 0.062, respectively) where ~1000 ambient supermicron aerosols contained 1 biological INP (the overall correlation with particles <1 µm was weaker but still significant at -20°C: pears = 0.57 with p = 0.004). By contrast, at -12 °C (Fig. 7b), the correlation with N_{sup} was less pronounced but still significant for days without rain (pears = 0.48 with p = 0.023), but not significant and weaker for rainy days (pears = 0.36 with p = 0.38) (and no overall correlation with particles <1 µm at -12°C: pears = 0.14 with p = 0.49). This suggests, as hypothesized above, that a small number and unique population of ice-active biological particles were aerosolized during and/or after rain events. Higher concentrations of biological INPs at -12 °C following rain qualitatively mimic increases in total INPs at -15 °C (in relation to supermicron particles) observed following precipitation by Mignani et al. (2021) at a Swiss alpine site. These observations counter expected increased scavenging and showed no relation to other aerosols in the expected size range of intact biological particles. High relative humidity may partially explain the highest biological INP concentrations at -12 °C on non-rainy days. Enhancements of high temperature INPs in general during wet conditions were in agreement with other past studies (Bigg et al., 2015; Elbert et al., 2007; Huffman et al., 2013; Wright et al., 2014), yet the mechanisms of emission of these particles remain unresolved.

The other organic INPs were noted as trending with the inorganic INPs (Fig. 3b), whether it rained or not (Figs. 5a and 5b). To investigate this, the correlation between other organic and inorganic INP concentrations at -25 °C, is presented in Figure 8a. Days with rain (before and during sampling) and days without rain showed similar behaviors: other organic INPs were

remarkably well correlated with the inorganic INPs (overall pears = 0.92 with p = 6×10^{-11}). The ratio was also fairly constant during the campaign. While the lowest concentrations of INPs tended to occur during rain events for these two populations, this did not affect the other organic/ inorganic INP ratio which was about 5.5 in average (σ = 3.4), while during days without rain it was 5.9 (σ = 4.3) at -25 °C. This suggests that other organic and inorganic INPs had the same general source and similar removal processes. By looking at their relations with aerosol number concentration, we found that inorganic INPs were well correlated with supermicron particles (Fig. 8b) (pears for rainy days = 0.99 with p = 3×10^{-6}, and for dry days = 0.90 with p = 2×10^{-3}, and 0.92 with p = 5×10^{-7} overall). By contrast, the correlation of inorganic INPs with submicron particles was weaker overall (Fig. 8c, pears = 0.53 with p = 0.004). Similar correlations occurred between other organic INPs and total aerosol number concentration. In general, the other organic and inorganic INPs appeared to be a linked population and primarily part of the supermicron aerosol population, probably from a single source such as soils.

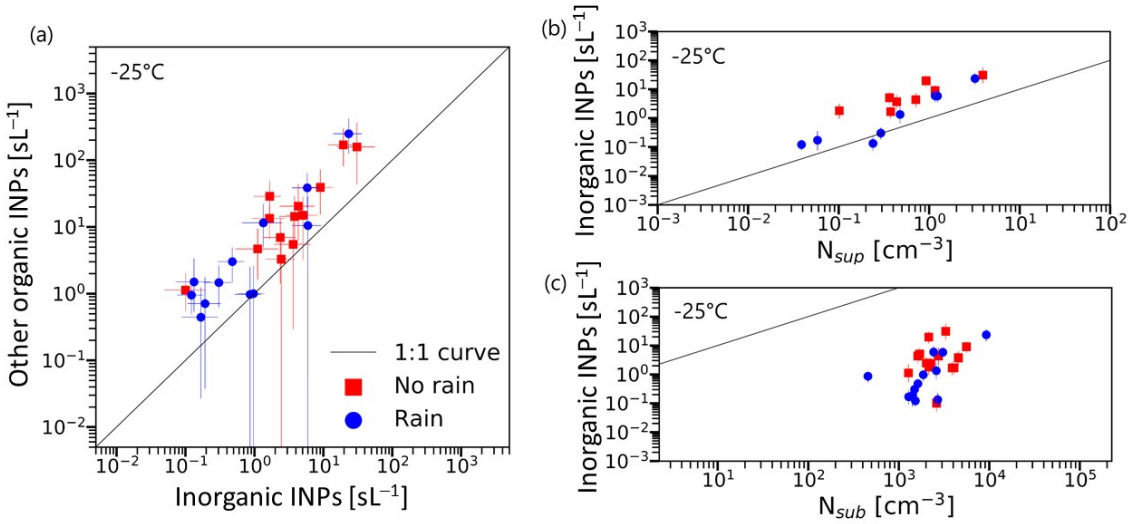

Figure 8. a) Concentration of other organic INPs versus inorganic INPs active at -25 °C during days with and without rain. b) Concentration of inorganic INPs active at -25 °C versus concentration of supermicron particles (N_{sup}) and c): versus concentration of submicron particles (N_{sub}). Panel (a) shares its legend with panels (b) and (c). Lines show 1:1 relationships.

While the other organic and inorganic INPs tends to act as a single population, they also modestly correlate with biological INPs, (Fig. S6 a-f). During rainy days, the correlation is maintained with biological INPs active at temperature around -15 °C, but not with biological INPs active at warmer temperatures, the latter showing enhanced concentrations. Hence, there may be two biological INP populations, one active at $T >$ ~ -15 °C, enhanced following rain events and under high RH (Fig. 7b), and one mostly active at lower temperatures (~ -20 °C), trending with other organic and inorganic INPs (Figs. S6a and S6d), potentially coming from similar sources, e.g., soil sources, as hypothesized above.

732

733 **3.4 INP relationships to regional soil particle composition and aerosol surface area**

734 **3.4.1 Single-particle composition and mixing state**

735 Given the frequency with which the air masses intercepted at AMF1 passed over the arable lands
736 to the east (Fig. 1), it is plausible that topsoil from cultivated fields was a principal source of
737 some INPs. Soil sample SDAr01, previously studied by Steinke et al. (2016) and by DeMott et
738 al. (2018), belongs to a unit that underlies the cultivated plain east of AMF1, where it forms a
739 north-south oriented, 100-300 km-wide band of haplic kastanozem soils. Below, we investigate
740 the single particle composition of this soil to assess whether this informs the observed activity
741 and the other organic/inorganic INP linkage described above. We revisit the ice nucleation
742 results for this sample for comparison to overall CACTI INPs in section 3.4.3.

743

744 Soil is a mixture of organic matter and mineral residues derived from the weathering of the local
745 basement rock, transported sediments and in-situ evaporite deposits. The LAAPTOF single
746 particle mass spectrometer can detect these materials from certain marker ions in the mass
747 spectra created after laser desorption ionization (LDI) of individual particles. Since the intensity
748 of these marker peaks is not quantitatively related to mass of material in the particle due to
749 matrix effects and the incomplete nature of the LDI process, compositional analysis is restricted
750 to the identification of particle composition types by comparing the mass spectra with well
751 characterized proxies.

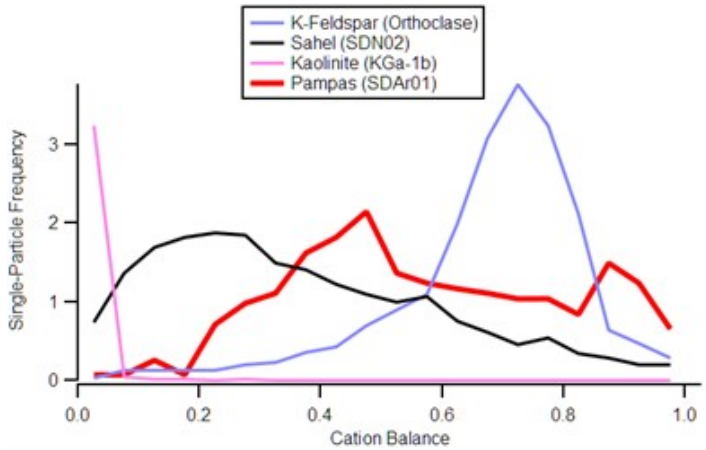

752

753 **Figure 9.** Cation balance (K+Na / Al+Si) of 325 single soil particles of SDAr01 by LAAPTOF
754 single particle mass spectrometry reveals it was somewhat higher than pure kaolinite, but lower
755 than pure K-Feldspar.

756

757 A suitable method for describing the soil dust properties of the pampas soil sample SDAr01 is to
758 compare the cation balance with defined proxies. A histogram of the cation balance from single
759 aerosolized particles of SDAr01 (Fig. 9) had a broad mode that was centered with a cation
760 balance lower than that of a pure K-feldspar (orthoclase $Ca_{0.01}Na_{0.25}K_{0.85}Si_{2.95}Al_{1.02}O_8$),
761 but much higher than that of pure kaolinite ($Al_2Si_2O_5(OH)_4$), the product of its weathering,
762 which should theoretically not contain alkali metals. The histogram for the SDAr01 sample
763 suggested the partial leaching of cations during weathering of alkali-rich precursor minerals,
764 such as feldspar, but also that the weathering process had not progressed to the formation of
765 kaolinite phase, such as observed in soils from the Sahel (Fig. 9). This indicated that SDAr01

had a composition which was consistent with an inter-continental setting for a source area rich in felsic minerals.

In addition to the cation balance, we also applied crystal structure analysis of SDAr01 alongside similar analyses for illite, K-Feldspar, Kaolinite and Sahel agricultural soils (Fig. 10). A number of this Pampas soil's particles plotted close to illite and K-Feldspar, but 63% of particles had crystal structure $\tau > 1$ (equation 2), which we interpreted as being somewhat amorphous, i.e., non-crystalline material (such as those produced from particles of crushed crystal), which may be recent deposition of volcanic ash or an amorphous matrix of clay with a felsic composition.

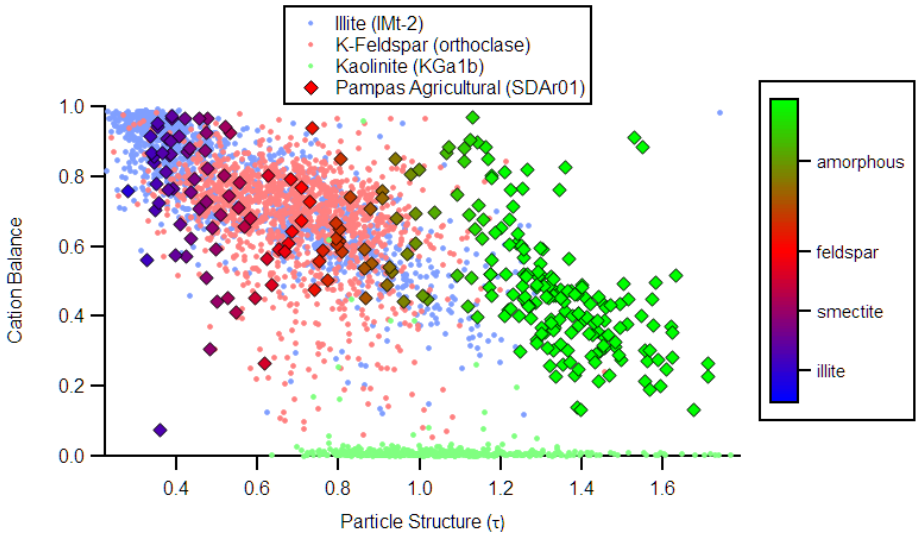

Figure 10. Cation balance versus crystal structure analysis ratio (τ) of 286 particles in pampas agricultural soil sample SDAr01 (larger diamonds, with black outlines) by LAAPTOF single-particle mass spectrometry. The color scale is our interpretation of particle mineralogy based on comparison with pure mineral proxies (colored dots), illite (IMt-2) and Kaolinite (KGa1b) from the clay mineral society, and K-Feldspar from a crushed crystal of orthoclase.

Single-particle mass spectrometry is also particularly useful for the investigation of the internal-mixing state of aerosol by using fragment ions in the negative ion spectra that are generated in tandem with the cations in each single-particle measurement. Commonly observed fragment ions in mineral dust particles are SO_4- and the organic/biological markers CN- and CNO-, none of which are derived from the silicate mineral, but are additional materials internally mixed into the single particle. As with the silicate composition, the fragment ion measurement is not quantitative with respect to primary compounds and is therefore best investigated with sub-composition analyses. For the analyses of the internally mixed organic/biological content, we used the organic mixing fraction CNO/(CNO + SO_4 + Cl), which effectively normalized the organic marker to the majority of the mixing state markers in each negative ion mass spectrum. The histogram of the organic mixing fraction indicated that all silicate particles contained some organic/biological material (Fig. 11) and that the amount of this material was relatively high compared to an agricultural soil from the Sahel, or a regosol (a weakly developed mineral soil) sampled from exposed rock in Morocco.

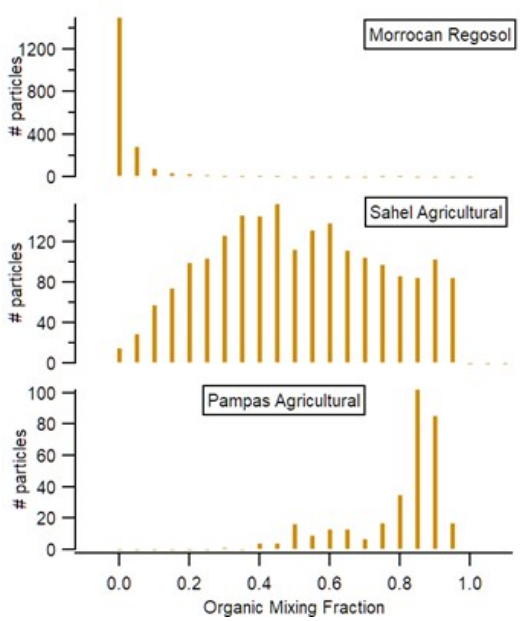

Figure 11. Internal mixing state of aerosolized soil samples analyzed by single-particle mass spectrometry. Organic mixing fraction is calculated from the CNO/(CNO + SO_4 + Cl) sub-composition analysis of negative ion marker peaks.

Overall, our online mass spectrometry analysis of the fine fraction of laboratory dispersed soil is consistent with previous offline studies of highly erodible agricultural soil rich in organic content (Lopez et al., 2007), with mineralogy of the clay fraction dominated by amorphous minerals (Hepper et al., 2006), along with argillized lithic and feldspar fragments from the crystalline basement, and detrital illite (Bonorino, 1966).

3.4.2 Normalization by aerosol surface area and consideration of the nature of inorganic INPs

The global mineral dust burden is composed of both primary minerals, mainly quartz and feldspar, and secondary minerals, such as clays (e.g., illite, kaolinite, chlorite, montmorillonite) (Murray et al., 2012, and references therein). Numerous studies have explored the immersion freezing ice nucleation abilities of mineral dusts from various regions, as well as characterizing single mineral types (see Kanji et al., 2017 and Murray et al., 2012), such as quartz, illite and felsic materials (Atkinson et al., 2013; Harrison et al., 2019; Hiranuma et al., 2015).

Since the single-particle mass spectrometry of the regionally-common SDAr01 soil sample found modest contributions from particles aligning with illite and K-Feldspar, here we attempt to explain the ice nucleation activity of the inorganic INP spectra observed at AMF1 by comparing them with parameterizations for these two minerals. A widely used metric for describing the ice nucleation activity of particles is the surface site density (hereafter $n_s(T)$), representing the number of ice nucleation active sites per unit of particle surface area at the processing temperature T (DeMott et al., 2015; Hoose and Möhler, 2012; Niemand et al., 2012). These active sites are conceptualized as specific locations on the INP surface that facilitate the formation of ice embryos by decreasing the activation energy necessary for the phase transition;

their nature is still poorly understood but they may occur preferentially at surface defects (Kiselev et al., 2017).

If one assumes that surface area alone controls the distribution of ice nucleation active sites, then $n_s(T)$ is derived from $n_{INP}(T)$, the total INP number concentration at the processing temperature T, with units of particles per unit of standard volume air, and the total aerosol surface area, S_{aer}, with units of m^2 per unit of standard volume air, according to:

$$n_s(T) = \frac{n_{INP}(T)}{S_{aer}} \quad (3)$$

This normalization is most appropriately applied to single INP types, with the assumption that at a given temperature, the number of active sites per unit of area does not change with particle size (Niemand et al., 2012). Other assumptions of this relation are that the INP type prevails in importance, while nucleation time plays a minor role. Here we applied this relationship to the inorganic portion of the CACTI INP spectra (Fig. 3b), assuming that they were representative of a common and relatively uniform mineralogical source. Further, we assumed that inorganic particles dominated the supermicron aerosol surface areas and that these surface areas were not significantly altered by the heat and peroxide treatments.

The aerosol number size distributions observed during the campaign had three typical size modes, reflecting different sources and physical processes (Figs. S5b and S5c). The smallest mode was centered around 50 nm (Aitken mode) and was observed in 80% of the measurements (size distributions measured every 5 min during the campaign). A second and less frequent mode, observed in 20% of the measurements, was centered around 200 nm (accumulation mode). The third, a coarse mode observed in all samples, started at approximately 0.7 μm (e.g., Fig. S5c) and was centered around 2 μm. A fourth mode, present in less than 1 % of the measurements, was localized between 4 μm and 10 μm and completely vanished during rainy days. Assuming that inorganic INPs were entirely minerals, they would more likely belong to the coarse modes (Dentener et al., 2006; Glaccum and Prospero, 1980; Perlwitz et al., 2015), which contributed significantly to the aerosol surface area and volume (Fig. S5a and S5c). Moreover, correlation analyses indicate that the total inorganic INP concentration trended with the supermicron aerosol surface area, while no correlation is evident with the surface area attributed to submicron particles (Figs. S7a and S7b).

The aerosol surface area distributions derived from the merged aerosol number size distributions (e.g., Fig. S5a) were integrated for particles above 1 μm in diameter to determine the supermicron surface areas used for normalization. After December 31, 2018, no APS data were available and we used nephelometer data to retrieve aerosol surface area for particles larger than 1 μm in aerodynamic diameter, as described in the Supporting Information. This aerodynamic diameter corresponds to a physical diameter ~0.75 μm. However, the surface area distributions generally had minima in the 0.7-1 μm size range (Figure S5a). Therefore, the inclusion of some smaller particles in the nephelometer-derived estimates of surface area is not expected to significantly increase the uncertainty of those estimates. Active site densities of inorganic INPs were then computed according to equation 3, where S_{aer} was set equal to the supermicron aerosol

surface areas. Comparison of the results with immersion freezing INP parameterizations is shown in Figure 12.

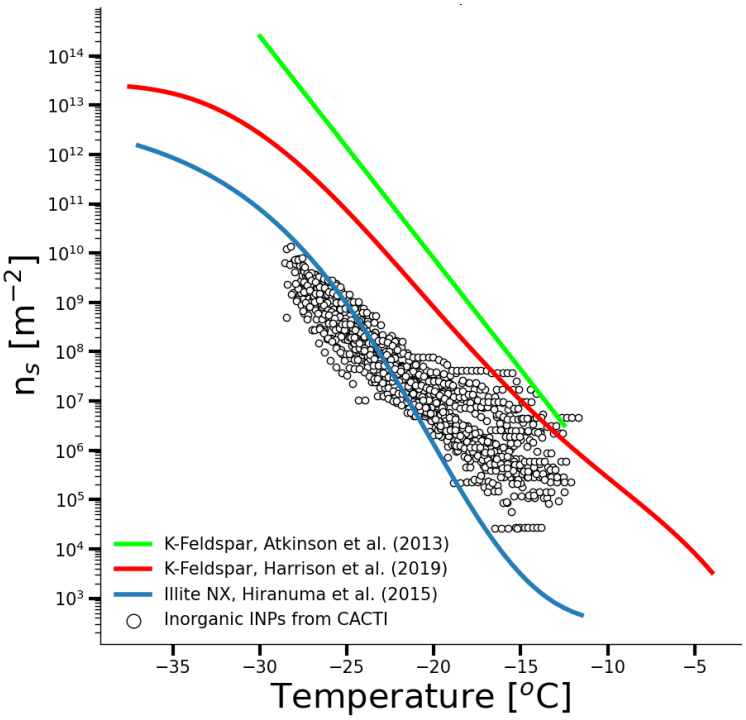

Figure 12. Ice-active surface site density of inorganic INPs measured in this study (open circles). Here, n_{INP} have been normalized using the total surface area of aerosols having a diameter >1.0 µm (see equation 3). INP parameterizations from Atkinson et al. (2013) and Harrison et al. (2019) were derived from Brunauer–Emmett–Teller (BET) gas adsorption surface measurements while aerosol surface areas in this study were derived by assuming spherical particles (geometric surface), likely underestimating the real surface area of the particles. Hence, the K-feldspar parameterizations were converted to estimated geometric surface area parameterizations, applying the conversion factor 2.6/0.89 used in DeMott et al. (2018) and derived from the K-feldspar sample used in their study. The uncertainties in n_s are not shown for clarity.

At lower temperatures, i.e. from -20 to -30 °C, the activity of the observed inorganic INPs most closely matched the illite NX parameterization from Hiranuma et al. (2015). Illite NX is actually an illite-rich proxy, containing >60% illite and a few percent of other atmospherically-relevant minerals, such as ~7% kaolinite and ~8% K-feldspar (see Murray et al., 2012). Above -20 °C, the number of active sites per m^2 positively diverged from the illite NX parameterization and approached the K-feldspar curve from Harrison et al. (2019).

As shown in Fig. 10, the single-particle crystal structure analysis of SDAr01 revealed it to be a continuum, with particles ranging in similarity from illite to K-feldspar to amorphous. Particles with the signature of illite were present and roughly equal in relative abundance to K-feldspar. This observation may underlie the agreement between the activity of the observed inorganic INPs and the illite NX parameterization. Crystal structure analysis also showed K-feldspar was present, but as a minor component, consistent with the surface site densities being significantly lower than INP parameterizations for pure K-feldspar (Atkinson et al., 2013; Harrison et al.,

2019). Indeed, the observed relative abundance of K-feldspar in the aerosolized SDAr01 particles supported the weighting of the total surface area of the supermicron aerosol by 0.2 (i.e., a K-feldspar surface fraction of 20%), as suggested by Harrison et al. (2019; c.f. Fig. 9). According to Atkinson et al. (2013) and Vergara-Temprado et al. (2017), a 0.2 weighting factor may better represent the K-feldspar fraction in the region. If applied to the results shown in Fig. 12, the reduced K-feldspar parameterization of Harrison et al. (2019) would align better with the derived inorganic n_s values from CACTI. However, the weighting would not modify the slope of the n_s, which would remain flatter than the Harrison et al. (2019) K-feldspar parameterization, perhaps due to the amorphous structure and mixed composition of many of the K-feldspar-like particles. Particle surface defects, such as cracks and cavities where nucleation is deemed to initiate, are likely less abundant on modestly aged particles, such as these observed in CACTI, compared to freshly milled materials commonly used in laboratory studies (Harrison et al., 2019). Differences in densities of such surface defects might also explain the lower slope of the inorganic INPs compared to the K-feldspar parameterization.

3.4.3 General surface area-based comparison of CACTI results and SDAr01

Analysis of the internal mixing states of aerosolized particles from SDAr01 showed a consistent and high fraction of organic material, in clear contrast to Morrocan regosol and Sahel agricultural soil (Fig. 11). Following equation 3, and again using the geometric surface areas of the supermicron aerosols, we derived n_s values for the untreated and heat treated INPs measured in CACTI. In Figure 13, we superimposed these with the n_s values derived from SDAr01 during FIN-02 (DeMott et al., 2018). Also included are results of new measurements following heating one of the SDAr01 samples from DeMott et al. (2018).

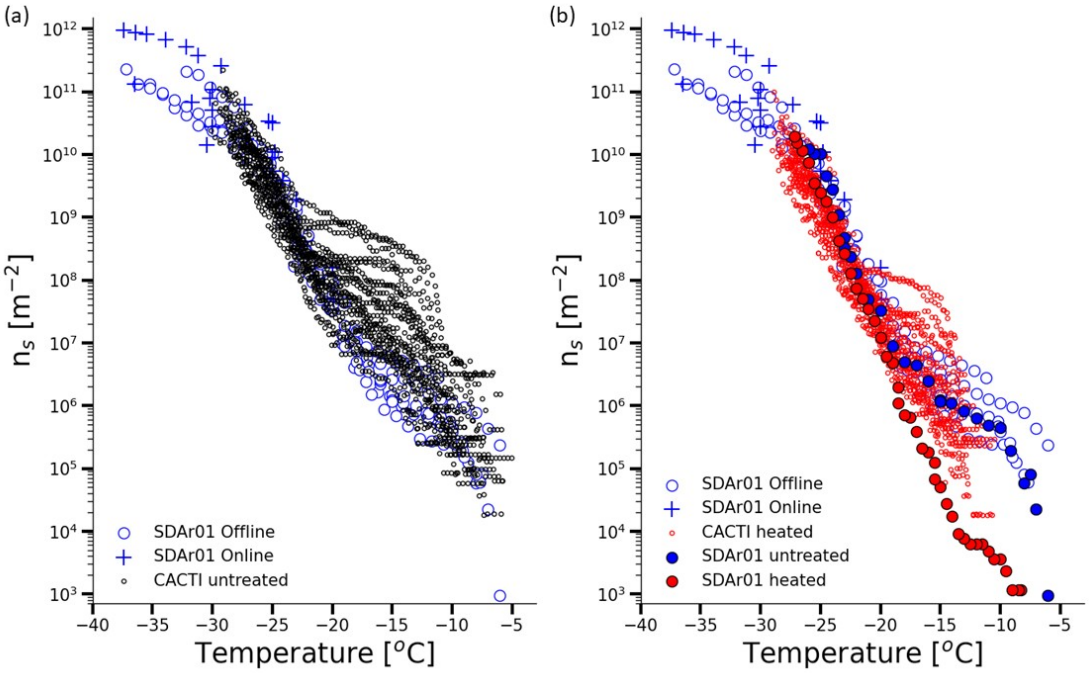

Figure 13. Surface site density of SDAr01 samples from the FIN-02 campaign (DeMott et al., 2018) plotted alongside the surface site density of a) the untreated INP spectra from this study, and b) the heat treated INPs from this study. The black outlined blue and red dots represent values of the untreated and heated SDAr01 sample.

The agreement between the untreated INP spectra and SDAr01 was remarkably good (Fig. 13a), especially below -22 °C where the other organic and inorganic INPs dominated the composition, strongly supporting the hypothesis that these linked populations (Fig. 8a) came mostly from the soil. Above -22 °C, the untreated spectra from CACTI showed a convex shape, positively diverging from the SDAr01 sample. This divergence was mostly due to the activity of the biological INPs. When these were removed from the comparison by using results post-heat treatment (Fig. 13b), the concordance between the CACTI and SDAr01 n_s spectra improved further. Treatment of the SDAr01 sample with heat revealed a dominance of biological INPs >-19 °C, but also a dominance of other organic/inorganic INPs below that, comparable to many spectra in Fig. 3a.

4 Conclusions

Our observations in central Argentina demonstrated that the local INP population active at temperatures from -5 to around -20 °C was largely dominated by biological INPs while below -22 °C, other organic (non-heat-labile organics) and inorganic INPs comprised the bulk of the population, although inorganic INPs were only a minor fraction of the total concentration. The population of biological INPs correlated with supermicron particle concentrations during days without rain and this correlation was strongest at lower temperatures. During rain events and under high relative humidity, the emission mechanisms appeared to be completely different from those dominating during dry days, and independent of the aerosol background concentration, particularly for biological INPs active at higher temperatures (i.e., -12 °C). Recent rainfall greatly increased the relative abundance of INPs active at high temperatures (the $[INP]_{-12°C}/[INP]_{-25°C}$ ratio) due to the simultaneous enhanced concentrations of the biological INPs and removal of the other INP classes from the boundary layer air, and/or a reduction of soil dust contributions due to the wet soil. After the rain, the ratio returned to the pre-rain value within one to 7 days.

Other organic and inorganic INPs were correlated with supermicron particle number concentrations during both rainy and non-rainy days, and were also strongly correlated with each other, suggesting they originated from the same source. The close agreement in n_s spectra between the CACTI field results and the DeMott et al. (2018) laboratory study of aerosolized particles from the regionally-common SDAr01 soil, supported by the findings from single-particle composition and mixing state that this soil contains K-feldspar, illite and a significant organic component (Figs. 10 and 11), builds a strong case that many INPs occurring in the boundary layer in CACTI were topsoil particles coming from the cultivated lands to the east. This accords with the general air flow patterns shown in the residence-time-weighted back-trajectories (Fig. 1). As an additional note, the results argue for the strong relevance of laboratory experiments for quantifying the behavior of soil-derived particles from a given region.

Of note, the derived ice-active site density also agrees with other soil INP parameterizations derived from very different agricultural regions, namely with Wyoming soil dust and English fertile soil dust (Tobo et al., 2014 and O'Sullivan et al., 2014 respectively, see Fig. 10b in DeMott et al., 2018). Therefore, the spectral signature derived from this study, as shown in Figure 13a, may in fact represent a typical agricultural soil signature, and not one specific to the Córdoba region. The predominance of biological INPs at temperatures above -20 °C emphasizes

the need for parameterization of this INP class, which should include their short-term variation caused by precipitation (e.g., fit parameterization derived by Mignani et al., 2021) and high relative humidity. Work to investigate whether the concentrations, characteristics and dynamics of the surface-level INPs are also applicable to observations at the altitude of clouds is ongoing (DeMott and Hill, 2020; Varble et al., 2021).

This study is the most comprehensive characterization of INPs in the boundary layer in Argentina, specifically to the east of the Sierras de Córdoba, to date. It is also a necessary first step toward improving understanding of aerosol impacts on convective clouds and precipitation formation in the province of Córdoba. We anticipate that this work will also inform a more general model of INPs found above continental agricultural landscapes through parameterization developments using similar data sets.

Data Availability

Data supporting the findings of this study are available from the following sources. All AOS data and original IS data files for the Cordoba AMF-1 deployment are available from the Department of Energy Atmospheric Radiation Measurement program website (https://www.arm.gov/data). Derived aerosol and ice spectrometer data products are available from the Mountain Scholar digital repository at Colorado State University (http://dx.doi.org/10.25675/10217/229310).

Competing Interests

The authors declare no competing interests.

Author Contributions

Conceptualization: P. J. DeMott, T. C. J. Hill, B. Testa, S. Kreidenweis, N. Marsden.
Data processing: B. Testa, T. C. J Hill, K. R. Barry, C. C. Hume, J. Uetake, H. Hare, R. J. Perkins.
Formal analysis: B. Testa, T. C. J. Hill, N. Marsden, Q. Bian.
Writing - review & editing: B. Testa, T. C. J. Hill, P. J. DeMott, S. M. Kreidenweis, N. Marsden, O. Möhler.

Acknowledgements

This study was supported by the Atmospheric System Research Program and Atmospheric Radiation Measurement Program sponsored by the U.S. Department of Energy (DOE), Office of Science, Office of Biological and Environmental Research (OBER), Climate and Environmental Sciences Division (CESD) under award numbers DE-SC0018929 and DE-SC0021116. Thanks to Roger Funk for details of the soil samples, ARM technicians Vagner Castro, Tércio Silva and Juarez Viegas responsible for sampling at AMF1, and the invaluable logistics support provided by Conrado Javier Rodriguez, Pablo Ariel Benitez and Julio Bourdin at INVAP Córdoba, and Tim Goering, Nita Patel and Heath Powers at LANL. María Julia Urbina is gratefully acknowledged for translation services and logistics support. The operation of the AIDA facility during the FIN-01 and FIN-02 campaigns was supported by the Helmholtz Association through the Research Program ATMO, and the German Science Foundation (DFG) through the research unit INUIT (FOR 1525, projects MO 668/4-1 and MO668/4-2). Thanks to the Master degree SOAC (Science of the Ocean, Atmosphere and Climate) from the University of Lyon for providing the framework of Baptiste Testa's internship with Colorado State University during

the conduct of this research. See Data Availability statement for access to data used in this manuscript.

References

Agresti, A., & Coull, B. A. (1998). Approximate Is Better than "Exact" for Interval Estimation of Binomial Proportions. *The American Statistician, 52*(2), 119-126. doi:10.2307/2685469

Ashbaugh, L. L., Malm, W. C., & Sadeh, W. Z. (1985). A residence time probability analysis of sulfur concentrations at grand Canyon National Park. *Atmospheric Environment (1967), 19*(8), 1263-1270. doi:https://doi.org/10.1016/0004-6981(85)90256-2

Atkinson, J. D., Murray, B. J., Woodhouse, M. T., Whale, T. F., Baustian, K. J., Carslaw, K. S., . . . Malkin, T. L. (2013). The importance of feldspar for ice nucleation by mineral dust in mixed-phase clouds. *Nature, 498*(7454), 355-358. doi:10.1038/nature12278

Barry, K. R., Hill, T. C. J., Jentzsch, C., Moffett, B. F., Stratmann, F., & DeMott, P. J. (2021). Pragmatic protocols for working cleanly when measuring ice nucleating particles. *Atmospheric Research, 250*, 105419. doi:https://doi.org/10.1016/j.atmosres.2020.105419

Barry, K. R., Hill, T. C. J., Levin, E. J. T., Twohy, C. H., Moore, K. A., Weller, Z. D., . . . DeMott, P. J. (2021). Observations of Ice Nucleating Particles in the Free Troposphere From Western US Wildfires. *Journal of Geophysical Research: Atmospheres, 126*(3), e2020JD033752. doi:https://doi.org/10.1029/2020JD033752

Beall, C. M., Stokes, M. D., Hill, T. C., DeMott, P. J., DeWald, J. T., & Prather, K. A. (2017). Automation and heat transfer characterization of immersion mode spectroscopy for analysis of ice nucleating particles. *Atmos. Meas. Tech., 10*(7), 2613-2626. doi:10.5194/amt-10-2613-2017

Bense, F., Costa, C., Oriolo, S., Löbens, S., Dunkl, I., Wemmer, K., & Siegesmund, S. (2017). Exhumation history and landscape evolution of the Sierra de San Luis (Sierras Pampeanas, Argentina) - new insights from low - temperature thermochronological data. *Andean Geology, 44*(3). doi:10.5027/andgeoV44n3-a0310.23689/fidgeo-2759

Bigg, E. K., Soubeyrand, S., & Morris, C. E. (2015). Persistent after-effects of heavy rain on concentrations of ice nuclei and rainfall suggest a biological cause. *Atmospheric Chemistry and Physics, 15*(5), 2313-2326. doi:10.5194/acp-15-2313-2015

Bohren, C. F., & Huffman, D. R. (1983). Absorption and Scattering by a Sphere. In *Absorption and Scattering of Light by Small Particles* (pp. 82-129).

Bonorino, G. F. (1966). Soil clay mineralogy of the Pampa plains, Argentina. *Journal of Sedimentary Research, 36*(4), 1026-1035. doi:10.1306/74d715eb-2b21-11d7-8648000102c1865d

Bullard, R. L., Uin, J., Springston, S. R., Kuang, C., & Smith, S. (2017). *Aerosol Inlet Characterization Experiment Report* (DOE/SC-ARM-TR-191). Retrieved from

Cabido, M., Zeballos, S. R., Zak, M., Carranza, M. L., Giorgis, M. A., Cantero, J. J., & Acosta, A. T. R. (2018). Native woody vegetation in central Argentina: Classification of Chaco and Espinal forests. *Applied Vegetation Science, 21*(2), 298-311. doi:https://doi.org/10.1111/avsc.12369

Cabrera, A. (1976). *Regiones Fitogeográficas Argentinas* (Vol. Enciclopedia Argentina de Agricultura y jardinería). Buenos Aires: Acme.

Chen, J., Wu, Z., Chen, J., Reicher, N., Fang, X., Rudich, Y., & Hu, M. (2021). Size-resolved atmospheric ice-nucleating particles during East Asian dust events. *Atmos. Chem. Phys., 21*(5), 3491-3506. doi:10.5194/acp-21-3491-2021

Claquin, T., & Schulz, M. (1999). Modeling the mineralogy of atmospheric dust sources. *Journal of Geophysical Research: Atmospheres, 104*(D18), 22243-22256. doi:https://doi.org/10.1029/1999JD900416

Conen, F., Morris, C. E., Leifeld, J., Yakutin, M. V., & Alewell, C. (2011). Biological residues define the ice nucleation properties of soil dust. *Atmos. Chem. Phys., 11*(18), 9643-9648. doi:10.5194/acp-11-9643-2011

Constantinidou, H., Hirano, S. S., Baker, L. S., & Upper, C. (1990). Atmospheric dispersal of ice nucleation-active Bacteria : the role of rain. *Phytopathology, 80*, 934-937.

Creamean, J. M., Mignani, C., Bukowiecki, N., & Conen, F. (2019). Using freezing spectra characteristics to identify ice-nucleating particle populations during the winter in the Alps. *Atmos. Chem. Phys., 19*(12), 8123-8140. doi:10.5194/acp-19-8123-2019

Dall'Osto, M., Harrison, R. M., Highwood, E. J., O'Dowd, C., Ceburnis, D., Querol, X., & Achterberg, E. P. (2010). Variation of the mixing state of Saharan dust particles with atmospheric transport. *Atmospheric Environment, 44*(26), 3135-3146. doi:https://doi.org/10.1016/j.atmosenv.2010.05.030

de Abelleyra, D., Banchero, S., Verón, S., Mosciaro, J., & Volante, J. (2019). *Mapa Nacional de Cultivos campaña 2018/2019* Retrieved from

de Boer, G., Morrison, H., Shupe, M. D., & Hildner, R. (2011). Evidence of liquid dependent ice nucleation in high-latitude stratiform clouds from surface remote sensors. *Geophysical Research Letters, 38*(1). doi:https://doi.org/10.1029/2010GL046016

DeMott, P. J., Hill, T. C., McCluskey, C. S., Prather, K. A., Collins, D. B., Sullivan, R. C., . . . Franc, G. D. (2016). Sea spray aerosol as a unique source of ice nucleating particles. *Proc Natl Acad Sci U S A, 113*(21), 5797-5803. doi:10.1073/pnas.1514034112

DeMott, P. J., Hill, T. C. J., Petters, M. D., Bertram, A. K., Tobo, Y., Mason, R. H., . . . Kreidenweis, S. M. (2017). Comparative measurements of ambient atmospheric concentrations of ice nucleating particles using multiple immersion freezing methods and a continuous flow diffusion chamber. *Atmospheric Chemistry and Physics, 17*(18), 11227-11245. doi:10.5194/acp-17-11227-2017

DeMott, P. J., Möhler, O., Cziczo, D. J., Hiranuma, N., Petters, M. D., Petters, S. S., . . . Zenker, J. (2018). The Fifth International Workshop on Ice Nucleation phase 2 (FIN-02): laboratory intercomparison of ice nucleation measurements. *Atmospheric Measurement Techniques, 11*(11), 6231-6257. doi:10.5194/amt-11-6231-2018

DeMott, P. J., & Prenni, A. J. (2010). New Directions: Need for defining the numbers and sources of biological aerosols acting as ice nuclei. *Atmospheric Environment, 44*(15), 1944-1945. doi:10.1016/j.atmosenv.2010.02.032

DeMott, P. J., Prenni, A. J., McMeeking, G. R., Sullivan, R. C., Petters, M. D., Tobo, Y., . . . Kreidenweis, S. M. (2015). Integrating laboratory and field data to quantify the immersion freezing ice nucleation activity of mineral dust particles. *Atmospheric Chemistry and Physics, 15*(1), 393-409. doi:10.5194/acp-15-393-2015

DeMott, P. J. a. T. C. H. (2020). *Cloud, Aerosol, and Complex Terrain Interactions (CACTI) ARM Aerial Facility (AAF) Measurements of Ice Nucleating Particles Field Campaign Report*. Retrieved from

Dentener, F., Kinne, S., Bond, T., Boucher, O., Cofala, J., Generoso, S., . . . Wilson, J. (2006). Emissions of primary aerosol and precursor gases in the years 2000 and 1750 prescribed data-sets for AeroCom. *Atmos. Chem. Phys., 6*(12), 4321-4344. doi:10.5194/acp-6-4321-2006

Després, V., Huffman, J. A., Burrows, S. M., Hoose, C., Safatov, A., Buryak, G., . . . Jaenicke, R. (2012). Primary biological aerosol particles in the atmosphere: a review. *Tellus B: Chemical and Physical Meteorology, 64*(1), 15598. doi:10.3402/tellusb.v64i0.15598

Diehl, K., Matthias-Maser, S., Jaenicke, R., & Mitra, S. K. (2002). The ice nucleating ability of pollen:: Part II. Laboratory studies in immersion and contact freezing modes. *Atmospheric Research, 61*(2), 125-133. doi:https://doi.org/10.1016/S0169-8095(01)00132-6

Elbert, W., Taylor, P. E., Andreae, M. O., & Pöschl, U. (2007). Contribution of fungi to primary biogenic aerosols in the atmosphere: wet and dry discharged spores, carbohydrates, and inorganic ions. *Atmos. Chem. Phys., 7*(17), 4569-4588. doi:10.5194/acp-7-4569-2007

Fan, J. W., Rosenfeld, D., Zhang, Y. W., Giangrande, S. E., Li, Z. Q., Machado, L. A. T., . . . de Souza, R. A. F. (2018). Substantial convection and precipitation enhancements by ultrafine aerosol particles. *Science, 359*(6374), 411-+. doi:10.1126/science.aan8461

Fan, J. W., Yuan, T. L., Comstock, J. M., Ghan, S., Khain, A., Leung, L. R., . . . Ovchinnikov, M. (2009). Dominant role by vertical wind shear in regulating aerosol effects on deep convective clouds. *Journal of Geophysical Research-Atmospheres, 114*, 9. doi:10.1029/2009jd012352

FAO-Unesco. (1971). *Soil map of the World*. South America

Field, P. R., Lawson, R. P., Brown, P. R. A., Lloyd, G., Westbrook, C., Moisseev, D., . . . Sullivan, S. (2017). Secondary Ice Production: Current State of the Science and Recommendations for the Future. In D. Baumgardner, G. M. McFarquhar, & A. J. Heymsfield (Eds.), *Ice Formation and Evolution in Clouds and Precipitation: Measurement and Modeling Challenges* (Vol. 58). Boston: Amer Meteorological Society.

Fridlind, A. M., Ackerman, A. S., Jensen, E. J., Heymsfield, A. J., Poellot, M. R., Stevens, D. E., . . . Rissman, T. A. (2004). Evidence for the predominance of mid-tropospheric aerosols as subtropical anvil cloud nuclei. *Science, 304*(5671), 718-722. doi:10.1126/science.1094947

Fröhlich-Nowoisky, J., Kampf, C. J., Weber, B., Huffman, J. A., Pöhlker, C., Andreae, M. O., . . . Pöschl, U. (2016). Bioaerosols in the Earth system: Climate, health, and ecosystem interactions. *Atmospheric Research, 182*, 346-376. doi:https://doi.org/10.1016/j.atmosres.2016.07.018

Gallavardin, S. J., Froyd, K. D., Lohmann, U., Moehler, O., Murphy, D. M., & Cziczo, D. J. (2008). Single Particle Laser Mass Spectrometry Applied to Differential Ice Nucleation Experiments at the AIDA Chamber. *Aerosol Science and Technology, 42*(9), 773-791. doi:10.1080/02786820802339538

Garcia, E., Hill, T. C. J., Prenni, A. J., DeMott, P. J., Franc, G. D., & Kreidenweis, S. M. (2012). Biogenic ice nuclei in boundary layer air over two U.S. High Plains agricultural regions. *Journal of Geophysical Research: Atmospheres, 117*(D18), n/a-n/a. doi:10.1029/2012jd018343

Gemayel, R., Hellebust, S., Temime-Roussel, B., Hayeck, N., Van Elteren, J. T., Wortham, H., & Gligorovski, S. (2016). The performance and the characterization of laser ablation aerosol particle time-of-flight mass spectrometry (LAAP-ToF-MS). *Atmos. Meas. Tech., 9*(4), 1947-1959. doi:10.5194/amt-9-1947-2016

Giorgis, M. A., Cingolani, A. M., Gurvich, D. E., Tecco, P. A., Chiapella, J., Chiarini, F., & Cabido, M. (2017). Changes in floristic composition and physiognomy are decoupled along elevation gradients in central Argentina. *Applied Vegetation Science, 20*(4), 558-571. doi:https://doi.org/10.1111/avsc.12324

Glaccum, R. A., & Prospero, J. M. (1980). Saharan aerosols over the tropical North Atlantic — Mineralogy. *Marine Geology, 37*(3), 295-321. doi:https://doi.org/10.1016/0025-3227(80)90107-3

Gong, X., Wex, H., Müller, T., Wiedensohler, A., Höhler, K., Kandler, K., . . . Stratmann, F. (2019). Characterization of aerosol properties at Cyprus, focusing on cloud condensation nuclei and ice-nucleating particles. *Atmos. Chem. Phys., 19*(16), 10883-10900. doi:10.5194/acp-19-10883-2019

Gute, E., & Abbatt, J. P. D. (2020). Ice nucleating behavior of different tree pollen in the immersion mode. *Atmospheric Environment, 231*, 117488. doi:https://doi.org/10.1016/j.atmosenv.2020.117488

Hand, J. L., & Kreidenweis, S. M. (2002). A New Method for Retrieving Particle Refractive Index and Effective Density from Aerosol Size Distribution Data. *Aerosol Science and Technology, 36*(10), 1012-1026. doi:10.1080/02786820290092276

Harrison, A. D., Lever, K., Sanchez-Marroquin, A., Holden, M. A., Whale, T. F., Tarn, M. D., . . . Murray, B. J. (2019). The ice-nucleating ability of quartz immersed in water and its atmospheric importance compared to K-feldspar. *Atmospheric Chemistry and Physics, 19*(17), 11343-11361. doi:10.5194/acp-19-11343-2019

Hassett, M. O., Fischer, M. W. F., & Money, N. P. (2015). Mushrooms as Rainmakers: How Spores Act as Nuclei for Raindrops. *PLoS One, 10*(10), e0140407-e0140407. doi:10.1371/journal.pone.0140407

Hepper, E. N., Buschiazzo, D. E., Hevia, G. G., Urioste, A., & Antón, L. (2006). Clay mineralogy, cation exchange capacity and specific surface area of loess soils with different volcanic ash contents. *Geoderma, 135*, 216-223. doi:https://doi.org/10.1016/j.geoderma.2005.12.005

Hill, T., DeMott, P., Conen, F., & Möhler, O. (2018). Impacts of Bioaerosols on Atmospheric Ice Nucleation Processes. In *Microbiology of Aerosols* (pp. 195-219).

Hill, T. C. J., DeMott, P. J., Tobo, Y., Fröhlich-Nowoisky, J., Moffett, B. F., Franc, G. D., & Kreidenweis, S. M. (2016). Sources of organic ice nucleating particles in soils. *Atmospheric Chemistry and Physics, 16*(11), 7195-7211. doi:10.5194/acp-16-7195-2016

Hirano, S. S., Baker, L. S., & Upper, C. D. (1996). Raindrop Momentum Triggers Growth of Leaf-Associated Populations of Pseudomonas syringae on Field-Grown Snap Bean Plants. *Appl Environ Microbiol, 62*(7), 2560-2566. doi:10.1128/aem.62.7.2560-2566.1996

Hiranuma, N., Adachi, K., Bell, D. M., Belosi, F., Beydoun, H., Bhaduri, B., . . . Möhler, O. (2019). A comprehensive characterization of ice nucleation by three different types of cellulose particles immersed in water. *Atmos. Chem. Phys., 19*(7), 4823-4849. doi:10.5194/acp-19-4823-2019

Hiranuma, N., Augustin-Bauditz, S., Bingemer, H., Budke, C., Curtius, J., Danielczok, A., . . . Yamashita, K. (2015). A comprehensive laboratory study on the immersion freezing behavior of illite NX particles: a comparison of 17 ice nucleation measurement techniques. *Atmospheric Chemistry and Physics, 15*(5), 2489-2518. doi:10.5194/acp-15-2489-2015

Hoose, C., & Möhler, O. (2012). Heterogeneous ice nucleation on atmospheric aerosols: a review of results from laboratory experiments. *Atmospheric Chemistry and Physics, 12*(20), 9817-9854. doi:10.5194/acp-12-9817-2012

Huang, S., Hu, W., Chen, J., Wu, Z., Zhang, D., & Fu, P. (2021). Overview of biological ice nucleating particles in the atmosphere. *Environ Int, 146*, 106197. doi:10.1016/j.envint.2020.106197

Huffman, J. A., Prenni, A. J., DeMott, P. J., Pöhlker, C., Mason, R. H., Robinson, N. H., . . . Pöschl, U. (2013). High concentrations of biological aerosol particles and ice nuclei during and after rain. *Atmospheric Chemistry and Physics, 13*(13), 6151-6164. doi:10.5194/acp-13-6151-2013

Hughes, D. D., Mampage, C. B. A., Jones, L. M., Liu, Z., & Stone, E. A. (2020). Characterization of Atmospheric Pollen Fragments during Springtime Thunderstorms. *Environmental Science & Technology Letters, 7*(6), 409-414. doi:10.1021/acs.estlett.0c00213

Joung, Y. S., Ge, Z., & Buie, C. R. (2017). Bioaerosol generation by raindrops on soil. *Nat Commun, 8*, 14668. doi:10.1038/ncomms14668

Kanji, Z. A., Ladino, L. A., Wex, H., Boose, Y., Burkert-Kohn, M., Cziczo, D. J., & Kramer, M. (2017). Overview of Ice Nucleating Particles. In D. Baumgardner, G. M. McFarquhar, & A. J. Heymsfield (Eds.), *Ice Formation and Evolution in Clouds and Precipitation: Measurement and Modeling Challenges* (Vol. 58). Boston: Amer Meteorological Society.

Keinert, A., Spannagel, D., Leisner, T., & Kiselev, A. (2020). Secondary Ice Production upon Freezing of Freely Falling Drizzle Droplets. *Journal of the Atmospheric Sciences, 77*(8), 2959-2967. doi:10.1175/jas-d-20-0081.1

Khain, A. P., BenMoshe, N., & Pokrovsky, A. (2008). Factors Determining the Impact of Aerosols on Surface Precipitation from Clouds: An Attempt at Classification. *Journal of the Atmospheric Sciences, 65*(6), 1721-1748. doi:10.1175/2007jas2515.1

Khlystov, A., Stanier, C., & Pandis, S. N. (2004). An Algorithm for Combining Electrical Mobility and Aerodynamic Size Distributions Data when Measuring Ambient Aerosol Special Issue ofAerosol Science and Technologyon Findings from the Fine Particulate Matter Supersites Program. *Aerosol Science and Technology, 38*(sup1), 229-238. doi:10.1080/02786820390229543

Kiselev, A., Bachmann, F., Pedevilla, P., Cox, S. J., Michaelides, A., Gerthsen, D., & Leisner, T. (2017). Active sites in heterogeneous ice nucleation—the example of K-rich feldspars. *Science, 355*(6323), 367-371. doi:10.1126/science.aai8034

Kupc, A., Williamson, C., Wagner, N. L., Richardson, M., & Brock, C. A. (2018). Modification, calibration, and performance of the Ultra-High Sensitivity Aerosol Spectrometer for particle size distribution and volatility measurements during the Atmospheric Tomography Mission (ATom) airborne campaign. *Atmos. Meas. Tech., 11*(1), 369-383. doi:10.5194/amt-11-369-2018

Kyrouac, J. (2019). *Aerosol Observing System Surface Meteorology (AOSMET) Instrument Handbook* (DOE/SC-ARM-TR-184 United States 10.2172/1573797 ORNL ORNL-ARM English). Retrieved from https://www.osti.gov/servlets/purl/1573797

L., C. M. (1976). Regiones Fitogeográficas Argentinas. In *Enciclopedia Argentina de agricultura y jardinería. Tomo II*. Buenos Aires, Argentina: Acme [In Spanish].

Ladino, L. A., Yakobi-Hancock, J. D., Kilthau, W. P., Mason, R. H., Si, M., Li, J., . . . Abbatt, J. P. D. (2016). Addressing the ice nucleating abilities of marine aerosol: A combination of deposition mode laboratory and field measurements. *Atmospheric Environment, 132*, 1-10. doi:https://doi.org/10.1016/j.atmosenv.2016.02.028

Langer, G., Morgan, G., Nagamoto, C. T., Solak, M., & Rosinski, J. (1979). Generation of Ice Nuclei in the Surface Outflow of Thunderstorms in Northeast Colorado. *Journal of Atmospheric Sciences, 36*(12), 2484-2494. doi:10.1175/1520-0469(1979)036<2484:Goinit>2.0.Co;2

Lauber, A., Kiselev, A., Pander, T., Handmann, P., & Leisner, T. (2018). Secondary Ice Formation during Freezing of Levitated Droplet. *Journal of the Atmospheric Sciences, 75*(8), 2815-2826. doi:10.1175/jas-d-18-0052.1

Lee, S. S., Donner, L. J., Phillips, V. T. J., & Ming, Y. (2008a). Examination of aerosol effects on precipitation in deep convective clouds during the 1997 ARM summer experiment. *Quarterly Journal of the Royal Meteorological Society, 134*(634), 1201-1220. doi:https://doi.org/10.1002/qj.287

Lee, S. S., Donner, L. J., Phillips, V. T. J., & Ming, Y. (2008b). The dependence of aerosol effects on clouds and precipitation on cloud-system organization, shear and stability. *Journal of Geophysical Research: Atmospheres, 113*(D16). doi:https://doi.org/10.1029/2007JD009224

López, M. L., & Ávila, E. E. (2013). Measurements of natural deposition ice nuclei in Córdoba, Argentina. *Atmospheric Chemistry and Physics, 13*(6), 3111-3119. doi:10.5194/acp-13-3111-2013

López, M. L., & Ávila, E. E. (2016). Influence of the ambient humidity on the concentration of natural deposition-mode ice-nucleating particles. *Atmos. Chem. Phys., 16*(2), 927-932. doi:10.5194/acp-16-927-2016

López, M. V., de Dios Herrero, J. M., Hevia, G. G., Gracia, R., & Buschiazzo, D. E. (2007). Determination of the wind-erodible fraction of soils using different methodologies. *Geoderma, 139*(3), 407-411. doi:https://doi.org/10.1016/j.geoderma.2007.03.006

Marinescu, P. J., van den Heever, S. C., Saleeby, S. M., Kreidenweis, S. M., & DeMott, P. J. (2017). The Microphysical Roles of Lower-Tropospheric versus Midtropospheric Aerosol Particles in Mature-Stage MCS Precipitation. *Journal of the Atmospheric Sciences, 74*(11), 3657-3678. doi:10.1175/jas-d-16-0361.1

Marsden, N., Flynn, M. J., Taylor, J. W., Allan, J. D., & Coe, H. (2016). Evaluating the influence of laser wavelength and detection stage geometry on optical detection efficiency in a single-particle mass spectrometer. *Atmos. Meas. Tech., 9*(12), 6051-6068. doi:10.5194/amt-9-6051-2016

Marsden, N. A., Flynn, M. J., Allan, J. D., & Coe, H. (2018). Online differentiation of mineral phase in aerosol particles by ion formation mechanism using a LAAP-TOF single-particle mass spectrometer. *Atmos. Meas. Tech., 11*(1), 195-213. doi:10.5194/amt-11-195-2018

Marsden, N. A., Ullrich, R., Möhler, O., Eriksen Hammer, S., Kandler, K., Cui, Z., . . . Coe, H. (2019). Mineralogy and mixing state of north African mineral dust by online single-particle mass spectrometry. *Atmos. Chem. Phys., 19*(4), 2259-2281. doi:10.5194/acp-19-2259-2019

McCluskey, C. S., DeMott, P. J., Prenni, A. J., Levin, E. J. T., McMeeking, G. R., Sullivan, A. P., . . . Kreidenweis, S. M. (2014). Characteristics of atmospheric ice nucleating particles associated with biomass burning in the US: Prescribed burns and wildfires. *Journal of Geophysical Research-Atmospheres, 119*(17), 13. doi:10.1002/2014jd021980

McCluskey, C. S., Hill, T. C. J., Humphries, R. S., Rauker, A. M., Moreau, S., Strutton, P. G., . . . DeMott, P. J. (2018). Observations of Ice Nucleating Particles Over Southern Ocean Waters. *Geophysical Research Letters, 45*(21), 11,989-911,997. doi:10.1029/2018gl079981

Mignani, C., Wieder, J., Sprenger, M. A., Kanji, Z. A., Henneberger, J., Alewell, C., & Conen, F. (2021). Towards parametrising atmospheric concentrations of ice nucleating particles active at moderate supercooling. *Atmos. Chem. Phys. Discuss., 2020*, 1-7. doi:10.5194/acp-2020-524

Mikutta, R., Kleber, M., Kaiser, K., & Jahn, R. (2005). Review: Organic Matter Removal from Soils using Hydrogen Peroxide, Sodium Hypochlorite, and Disodium Peroxodisulfate. *Soil Science Society of America Journal, 69*(1), 120-135. doi:https://doi.org/10.2136/sssaj2005.0120

Mülmenstädt, J., Sourdeval, O., Delanoë, J., & Quaas, J. (2015). Frequency of occurrence of rain from liquid-, mixed-, and ice-phase clouds derived from A-Train satellite retrievals. *Geophysical Research Letters, 42*(15), 6502-6509. doi:10.1002/2015gl064604

Murphy, D. M. (2007). The design of single particle laser mass spectrometers. *Mass Spectrometry Reviews, 26*(2), 150-165. doi:https://doi.org/10.1002/mas.20113

Murray, B. J., O'Sullivan, D., Atkinson, J. D., & Webb, M. E. (2012). Ice nucleation by particles immersed in supercooled cloud droplets. *Chem Soc Rev, 41*(19), 6519-6554. doi:10.1039/c2cs35200a

Nelder, J. A., & Mead, R. (1965). A Simplex Method for Function Minimization. *The Computer Journal, 7*(4), 308-313. doi:10.1093/comjnl/7.4.308

Niemand, M., Möhler, O., Vogel, B., Vogel, H., Hoose, C., Connolly, P., . . . Leisner, T. (2012). A Particle-Surface-Area-Based Parameterization of Immersion Freezing on Desert Dust Particles. *Journal of the Atmospheric Sciences, 69*(10), 3077-3092. doi:10.1175/JAS-D-11-0249.1

O'Sullivan, D., Adams, M. P., Tarn, M. D., Harrison, A. D., Vergara-Temprado, J., Porter, G. C. E., . . . Murray, B. J. (2018). Contributions of biogenic material to the atmospheric ice-nucleating particle population in North Western Europe. *Sci Rep, 8*(1), 13821. doi:10.1038/s41598-018-31981-7

O'Sullivan, D., Murray, B. J., Malkin, T. L., Whale, T. F., Umo, N. S., Atkinson, J. D., . . . Webb, M. E. (2014). Ice nucleation by fertile soil dusts: relative importance of mineral and biogenic components. *Atmospheric Chemistry and Physics, 14*(4), 1853-1867. doi:10.5194/acp-14-1853-2014

Perlwitz, J. P., Pérez García-Pando, C., & Miller, R. L. (2015). Predicting the mineral composition of dust aerosols – Part 1: Representing key processes. *Atmos. Chem. Phys., 15*(20), 11593-11627. doi:10.5194/acp-15-11593-2015

Petters, M. D., & Wright, T. P. (2015). Revisiting ice nucleation from precipitation samples. *Geophysical Research Letters, 42*(20), 8758-8766. doi:https://doi.org/10.1002/2015GL065733

Phillips, V. T. J., Yano, J. I., Formenton, M., Ilotoviz, E., Kanawade, V., Kudzotsa, I., . . . Tessendorf, S. A. (2017). Ice Multiplication by Breakup in Ice-Ice Collisions. Part II: Numerical Simulations. *Journal of the Atmospheric Sciences, 74*(9), 2789-2811. doi:10.1175/jas-d-16-0223.1

Prenni, A. J., Tobo, Y., Garcia, E., DeMott, P. J., Huffman, J. A., McCluskey, C. S., . . . Pöschl, U. (2013). The impact of rain on ice nuclei populations at a forested site in Colorado. *Geophysical Research Letters, 40*(1), 227-231. doi:10.1029/2012gl053953

Price, H. C., Baustian, K. J., McQuaid, J. B., Blyth, A., Bower, K. N., Choularton, T., . . . Murray, B. J. (2018). Atmospheric Ice-Nucleating Particles in the Dusty Tropical Atlantic. *Journal of Geophysical Research: Atmospheres, 123*(4), 2175-2193. doi:https://doi.org/10.1002/2017JD027560

Pruppacher, H. R., & Klett, J. D. (1997). *Microphysics of Clouds and Precipitation* (2 ed.): Springer, Dordrecht.

Pummer, B. G., Bauer, H., Bernardi, J., Bleicher, S., & Grothe, H. (2012). Suspendable macromolecules are responsible for ice nucleation activity of birch and conifer pollen. *Atmos. Chem. Phys., 12*(5), 2541-2550. doi:10.5194/acp-12-2541-2012

Rasmussen, K. L., Zuluaga, M. D., & Houze Jr., R. A. (2014). Severe convection and lightning in subtropical South America. *Geophysical Research Letters, 41*(20), 7359-7366. doi:https://doi.org/10.1002/2014GL061767

Reinard, M. S., & Johnston, M. V. (2008). Ion formation mechanism in laser desorption ionization of individual nanoparticles. *Journal of the American Society for Mass Spectrometry, 19*(3), 389-399. doi:10.1021/jasms.8b03150

Rolph, G., Stein, A., & Stunder, B. (2017). Real-time Environmental Applications and Display sYstem: READY. *Environmental Modelling & Software, 95*, 210-228. doi:https://doi.org/10.1016/j.envsoft.2017.06.025

Schiebel, T. (2017). *Ice Nucleation Activity of Soil Dust Aerosols*.

Schill, G. P., DeMott, P. J., Emerson, E. W., Rauker, A. M. C., Kodros, J. K., Suski, K. J., . . . Kreidenweis, S. M. (2020). The contribution of black carbon to global ice nucleating particle concentrations relevant to mixed-phase clouds. *Proceedings of the National Academy of Sciences, 117*(37), 22705-22711. doi:10.1073/pnas.2001674117

Schneider, J., Höhler, K., Heikkilä, P., Keskinen, J., Bertozzi, B., Bogert, P., . . . Möhler, O. (2021). The seasonal cycle of ice-nucleating particles linked to the abundance of biogenic aerosol in boreal forests. *Atmos. Chem. Phys., 21*(5), 3899-3918. doi:10.5194/acp-21-3899-2021

Siegmund, N., Funk, R., Koszinsky, S., Buschiazzo, D. E., & Sommer, M. (2018). Effects of low-scale landscape structures on aeolian transport processes on arable land. *Aeolian Research, 32*, 181-191. doi:https://doi.org/10.1016/j.aeolia.2018.03.003

Sotiropoulou, G., Vignon, É., Young, G., Morrison, H., O'Shea, S. J., Lachlan-Cope, T., . . . Nenes, A. (2021). Secondary ice production in summer clouds over the Antarctic coast: an underappreciated process in atmospheric models. *Atmos. Chem. Phys., 21*(2), 755-771. doi:10.5194/acp-21-755-2021

Sprent, P. (2011). Fisher Exact Test. In M. Lovric (Ed.), *International Encyclopedia of Statistical Science* (pp. 524-525). Berlin, Heidelberg: Springer Berlin Heidelberg.

Steenken, A., Siegesmund, S., López de Luchi, M. G., Frei, R., & Wemmer, K. (2006). Neoproterozoic to Early Palaeozoic events in the Sierra de San Luis: implications for the Famatinian geodynamics in the Eastern Sierras Pampeanas (Argentina). *Journal of the Geological Society, 163*(6), 965-982. doi:10.1144/0016-76492005-064

Steenken, A., Wemmer, K., Martino, R. D., López de Luchi, M. G., Guereschi, A. & Siegesmund, S. (2010). Post-Pampean cooling and the uplift of the Sierras Pampeanas in the west of Córdoba (Central Argentina). *N. Jb. Geol. Paläont. Abh., 256, 235–255*. doi:https://doi.org/10.1127/0077-7749/2010/0094

Stein, A. F., Draxler, R. R., Rolph, G. D., Stunder, B. J. B., Cohen, M. D., & Ngan, F. (2015). NOAA's HYSPLIT Atmospheric Transport and Dispersion Modeling System. *Bulletin of the American Meteorological Society, 96*(12), 2059-2077. doi:10.1175/bams-d-14-00110.1

Steinke, I., Funk, R., Busse, J., Iturri, A., Kirchen, S., Leue, M., . . . Leisner, T. (2016). Ice nucleation activity of agricultural soil dust aerosols from Mongolia, Argentina, and Germany. *Journal of Geophysical Research: Atmospheres, 121*(22), 13,559-513,576. doi:10.1002/2016jd025160

Storer, R. L., & Van den Heever, S. C. (2013). Microphysical Processes Evident in Aerosol Forcing of Tropical Deep Convective Clouds. *Journal of the Atmospheric Sciences, 70*(2), 430-446. doi:10.1175/jas-d-12-076.1

Storer, R. L., van den Heever, S. C., & Stephens, G. L. (2010). Modeling Aerosol Impacts on Convective Storms in Different Environments. *Journal of the Atmospheric Sciences, 67*(12), 3904-3915. doi:10.1175/2010jas3363.1

Suski, K. J., Hill, T. C. J., Levin, E. J. T., Miller, A., DeMott, P. J., & Kreidenweis, S. M. (2018). Agricultural harvesting emissions of ice-nucleating particles. *Atmospheric Chemistry and Physics, 18*(18), 13755-13771. doi:10.5194/acp-18-13755-2018

Teruggi, M. E. (1957). The nature and origin of Argentine loess. *Journal of Sedimentary Research, 27*(3), 322-332. doi:10.1306/74d706dc-2b21-11d7-8648000102c1865d

Tobo, Y., DeMott, P. J., Hill, T. C. J., Prenni, A. J., Swoboda-Colberg, N. G., Franc, G. D., & Kreidenweis, S. M. (2014). Organic matter matters for ice nuclei of agricultural soil origin. *Atmospheric Chemistry and Physics, 14*(16), 8521-8531. doi:10.5194/acp-14-8521-2014

Tobo, Y., Prenni, A. J., DeMott, P. J., Huffman, J. A., McCluskey, C. S., Tian, G., . . . Kreidenweis, S. M. (2013). Biological aerosol particles as a key determinant of ice nuclei populations in a forest ecosystem. *Journal of Geophysical Research: Atmospheres, 118*(17), 10,100-110,110. doi:10.1002/jgrd.50801

Tomlin, J. M., Jankowski, K. A., Rivera-Adorno, F. A., Fraund, M., China, S., Stirm, B. H., . . . Laskin, A. (2020). Chemical Imaging of Fine Mode Atmospheric Particles Collected from a Research Aircraft over Agricultural Fields. *ACS Earth and Space Chemistry, 4*(11), 2171-2184. doi:10.1021/acsearthspacechem.0c00172

Uin, J., Aiken, A. C., Dubey, M. K., Kuang, C., Pekour, M., Salwen, C., . . . Springston, S. R. (2019). Atmospheric Radiation Measurement (ARM) Aerosol Observing Systems (AOS) for Surface-Based In Situ Atmospheric Aerosol and Trace Gas Measurements. *Journal of Atmospheric and Oceanic Technology, 36*(12), 2429-2447. doi:10.1175/JTECH-D-19-0077.1

Uin, J., & Smith, S. (2020). *Southern Great Plains (SGP) Aerosol Observing System (AOS) Instrument Handbook* Retrieved from

Ullrich, R., Hoose, C., Möhler, O., Niemand, M., Wagner, R., Höhler, K., . . . Leisner, T. (2017). A New Ice Nucleation Active Site Parameterization for Desert Dust and Soot. *Journal of the Atmospheric Sciences, 74*(3), 699-717. doi:10.1175/jas-d-16-0074.1

Vali, G. (1971). Quantitative Evaluation of Experimental Results an the Heterogeneous Freezing Nucleation of Supercooled Liquids. *Journal of Atmospheric Sciences, 28*(3), 402-409. doi:10.1175/1520-0469(1971)028<0402:Qeoera>2.0.Co;2

Vali, G., DeMott, P. J., Möhler, O., & Whale, T. F. (2015). Technical Note: A proposal for ice nucleation terminology. *Atmos. Chem. Phys., 15*(18), 10263-10270. doi:10.5194/acp-15-10263-2015

van den Heever, S. C., Carrio, G. G., Cotton, W. R., DeMott, P. J., & Prenni, A. J. (2006). Impacts of nucleating aerosol on Florida storms. Part I: Mesoscale simulations. *Journal of the Atmospheric Sciences, 63*(7), 1752-1775. doi:10.1175/jas3713.1

Van Den Heever, S. C., & Cotton, W. R. (2007). Urban aerosol impacts on downwind convective storms. *Journal of Applied Meteorology and Climatology, 46*(6), 828-850. doi:10.1175/jam2492.1

Varble, A., Nesbitt, S., Salio, P., Hardin, J., Borque, P., DeMott, P., . . . Zipser, E. (2021). Utilizing a Storm-Generating Hotspot to Study Convective Cloud Transitions: The CACTI Experiment. *Bulletin of the American Meteorological Society*. doi: 10.1175/BAMS-D-20-0030.1

Vergara-Temprado, J., Murray, B. J., Wilson, T. W., O'Sullivan, D., Browse, J., Pringle, K. J., . . . Carslaw, K. S. (2017). Contribution of feldspar and marine organic aerosols to global ice nucleating particle concentrations. *Atmos. Chem. Phys., 17*(5), 3637-3658. doi:10.5194/acp-17-3637-2017

Wang, B., Harder, T. H., Kelly, S. T., Piens, D. S., China, S., Kovarik, L., . . . Laskin, A. (2016). Airborne soil organic particles generated by precipitation. *Nature Geoscience, 9*(6), 433-437. doi:10.1038/ngeo2705

Wilson, T. W., Ladino, L. A., Alpert, P. A., Breckels, M. N., Brooks, I. M., Browse, J., . . . Murray, B. J. (2015). A marine biogenic source of atmospheric ice-nucleating particles. *Nature, 525*(7568), 234-238. doi:10.1038/nature14986

Winker, D. M., Tackett, J. L., Getzewich, B. J., Liu, Z., Vaughan, M. A., & Rogers, R. R. (2013). The global 3-D distribution of tropospheric aerosols as characterized by CALIOP. *Atmos. Chem. Phys., 13*(6), 3345-3361. doi:10.5194/acp-13-3345-2013

Wright, T. P., Hader, J. D., McMeeking, G. R., & Petters, M. D. (2014). High Relative Humidity as a Trigger for Widespread Release of Ice Nuclei. *Aerosol Science and Technology, 48*(11), i-v. doi:10.1080/02786826.2014.968244

Yu, H., Fu, R., Dickinson, R. E., Zhang, Y., Chen, M., & Wang, H. (2007). Interannual variability of smoke and warm cloud relationships in the Amazon as inferred from MODIS retrievals. *Remote Sensing of Environment, 111*(4), 435-449. doi:https://doi.org/10.1016/j.rse.2007.04.003

Zipser, E. J., Cecil, D. J., Liu, C., Nesbitt, S. W., & Yorty, D. P. (2006). WHERE ARE THE MOST INTENSE THUNDERSTORMS ON EARTH? *Bulletin of the American Meteorological Society, 87*(8), 1057-1072. doi:10.1175/bams-87-8-1057